

Vol2 No1
January 2022
e-ISSN: 2682-9177

AJMed TECH ASIAN JOURNAL OF MEDICAL TECHNOLOGY

<https://doi.org/10.32896/ajmedtech.v2n1>



Intracranial hemorrhage detection in ct scan using deep learning
Thermo-pneumatic micropump for drug delivery applications
Smart health monitoring system utilizing internet of things (iot) and arduino
Dose mapping of gamma irradiation chamber (gic)

<https://ajmedtech.com>



Editorial Team

Editor-in-Chief

Prof. Dr. Ahmad Sobri Muda (Malaysia); Medical
Assoc. Prof. Ir. Ts. Dr. Abdul Rahim Abdullah (Malaysia); Technology

Managing Editor

Ts. Dr. Norhashimah Mohd Saad (Malaysia)
Assoc. Prof. Dr. Noramaliza Mohd Noor (Malaysia)

Editorial Board

Ir. Dr. Anis Suhaila Shuib (Malaysia)
Dr. Norihan Abdul Hamid (Malaysia)
Assoc. Prof. Dr. Wira Hidayat Mohd Saad
(Malaysia)
Dr. Norhidayah Mohamad Yatim (Malaysia)
Dr. Anas Tharek (Malaysia)
Mr. Adam Samsudin (Malaysia)
Mrs. Kamilah Jaffar (Malaysia)
Dr. Mohd Hatta Jopri (Malaysia)
Dr. Ezreen Farina Shair (Malaysia)

ASIAN JOURNAL OF MEDICAL TECHNOLOGY

Contents

Volume 2

Number 1

January 2022

| <i>No.</i> | <i>Title</i> | <i>Page</i> |
|------------|--|-------------|
| 1. | INTRACRANIAL HEMORRHAGE DETECTION IN CT SCAN USING DEEP LEARNING <i>A. Tharek, A. S. Muda, A. B. Hudi, A. B. Hudin.....</i> | <i>1</i> |
| 2. | THERMO-PNEUMATIC MICROPUMP FOR DRUG DELIVERY APPLICATIONS <i>N. Hamid, B.Y Majlis, J Yunas, M. Ibrahim.....</i> | <i>19</i> |
| 3. | SMART HEALTH MONITORING SYSTEM UTILIZING INTERNET OF THINGS (IoT) AND ARDUINO <i>A. Mihat, N. Mohd Saad, E. F. Shair, A. B. Nasir Aslam, R. Abdul Rahim.....</i> | <i>35</i> |
| 4. | DOSE MAPPING OF GAMMA IRRADIATION CHAMBER (GIC) <i>N. Mohd Noor, M. A. A. Mohd Roslee, N. A. Ahmad, N. S. Sohini.....</i> | <i>49</i> |

balt solutions

for AVM treatment

squid
EVOH co-polymer



sonic

detachable tip microcatheter



Join us for Hands-On
AVM Workshops. Register your interest with
carlteh@medcinpharma.com / hiba@medcinpharma.com

SQUID is a non-adhesive liquid embolic agent indicated for embolization of lesions in the peripheral and neurovasculature, including arteriovenous malformations and hypervascular tumors. Class III CE 0459 in compliance with Medical Device Directive (MDD 93/42/EEC amended by 2007/47/ EC. Manufactured by EMBO-FLUSSIGKEITEN AG, Route des Avouillons 30, CH-1196 GLAND, Switzerland. Carefully read the instruction of use before use. First CE marking:2012. SONIC is a reinforced microcatheter indicated in selective and hyperselective vascular catheterization for diagnostic or therapeutic purposes. Class III CE 0459 in compliance with Medical Device Directive (MDD 93/42/EEC amended by 2007/47/ EC. Manufactured by BALT Extrusion. Carefully read the instruction of use before use. First CE marking:2012. The content of this document, in particular data, information, trademarks and logos is BALT SAS's sole property. © 2018 BALT SAS and affiliates, all rights reserved. All representation and/or reproduction, whether in part or in full, is forbidden and would be considered a violation of BALT SAS and its affiliates' copyrights and other intellectual proprietary rights. This document with associated pictures is non-contractual and is solely dedicated to healthcare professionals and BALT's distributors (BALT's supplier's distributors). The products commercialized by BALT shall exclusively be used in accordance with the instructions for use included in the boxes.



MEDCIN PHARMA SDN BHD (587084-D)

Imported and distributed by :

Medcin Pharma Sdn Bhd (587084-D)
H-G-3A, Blok H, Sekitar 26 Enterprise,
Persiaran Hulu Selangor, Seksyen 26,
40400 Shah Alam, Selangor Darul Ehsan
Tel: +60 (03) 5192 3966
Fax: +60 (03) 5191 9539
<http://www.medcinpharma.com>

INTRACRANIAL HEMORRHAGE DETECTION IN CT SCAN USING DEEP LEARNING

Anas Tharek¹, Ahmad Sobri Muda^{1,*}, Aqilah Baseri Hudi², and Azzam Baseri Hudin³

¹Universiti Putra Malaysia, Serdang, 43400, Selangor, Malaysia.

^{2,3}Universiti Kebangsaan Malaysia, Bangi, 43600, Selangor, Malaysia.

*Corresponding Author's Email: asobri@upm.edu.my

Article History: Received December 2, 2021; Revised January 9, 2022;
Accepted January 9, 2022

ABSTRACT: Missed detection of intracranial hemorrhage in Head CT scans has significantly impacted patient morbidity and mortality. Early detection of intracranial hemorrhage enables patients to receive appropriate treatment which resulted in a better outcome. Some doctors have limited experience in interpreting the CT scan hence increasing the probability to miss the hemorrhage. The main objective of this study is to develop an algorithm model capable of detecting intracranial hemorrhage in a head CT scan. We are using deep learning from a convolutional neural network (CNN) to produce this algorithm module. This was a cross-sectional study using secondary data, in which 200 data were collected from public datasets. All of the samples have been anonymized into secondary data. The algorithm model is trained using deep learning via a Jupyter Notebook platform. To analyze the algorithm model performance, a confusion matrix was used to measure the accuracy, sensitivity, specificity, precision, and F1 score. This study showed that from 200 training data, 95 samples were true positive, 95 samples were true negative, 7 samples were false positive, and 3 samples were false negative. This algorithm model shows high sensitivity (0.9694), high specificity (0.9314), high precision (0.9314), and high accuracy (0.9500) with an F1 score of 0.9500. This study has proven that deep learning by using CNN enables us to create an accurate classifier that can differentiate between head CT scan with intracranial hemorrhage and without hemorrhage.

KEYWORDS: *Artificial intelligence, deep learning, convolutional neural network, intracranial hemorrhage, CT Brain.*

1.0 INTRODUCTION

Intracranial hemorrhage is a potentially life-threatening neurological condition. It results in a significant burden on health resources. It can happen in many different causes such as due to increased blood pressure, hemorrhage secondary to infarct, trauma, tumor hemorrhage, and many more. One of the common causes of intracranial hemorrhage is traumatic brain injury[1]. When the blood from trauma is in contact with adjacent brain tissues, it irritates and causes swelling. This is known as cerebral edema. The pool of blood within the brain parenchyma is called a hematoma. This causes increased pressure on the adjacent brain tissues which leads to reduced blood flow and kills the brain cells [2].

There are four types of intracranial hemorrhage in trauma characterized by the extravascular accumulation of blood within different intracranial spaces. There are extradural hemorrhage (EDH), subdural hemorrhage (SDH), subarachnoid hemorrhage (SAH), and contusional hemorrhage [3]. Extradural hemorrhage is also known as epidural hemorrhage which is a collection of blood in between the inner surface of the skull and the outer surface of the dura. This is usually associated with a skull fracture. The Source of bleeding is usually from the artery, most commonly the middle meningeal artery. Subdural hemorrhage is a collection of blood within the subdural spaces which is the potential space between the dura and arachnoid of meninges around the brain. Prognosis varies widely depending on the size and chronicity of the hemorrhage. Subarachnoid hemorrhage (SAH) is a type of extra-axial intracranial hemorrhage located within the subarachnoid spaces. Besides trauma, other causes that can lead to subarachnoid hemorrhage are ruptured aneurysm, venous infarction, cerebral vasculitis, and dural arteriovenous malformation. Contusional hemorrhage is a type of intra-axial intracranial hemorrhage which is commonly seen in the setting of significant head injury. It is characterized by foci of hemorrhage in the brain parenchymal which frequently happens in the frontal lobes.

When a patient comes to the hospital after trauma. The emergency department will assess the patient. The detailed neurological examination must be completed after primary and secondary surveys were done. Not all trauma cases need a CT Scan due to radiation risk. NICE (national institute for health and care excellence) has made a guideline to choose which patient requires a CT scan done as the benefit outweighs the risk of radiation [4].

Once the CT scan is done, the radiology doctor will review the case. In normal situations, not all cases are being reviewed at the same time the scan was done as they need to handle other modalities in the radiology department. The primary team is the one who usually sees the scan first. In some of the cases, subtle intracranial hemorrhage may be missed by them. This is due to the highly variable appearance of intracranial hemorrhage, depending on its age and location. The most common types of intracranial hemorrhage that were missed were subdural and subarachnoid hemorrhage occurring in 39% and 33% of the cases, respectively. The most common location for missed subdural hemorrhage was either parafalcine or frontal [5].

Rapid diagnosis and management of patients with intracranial hemorrhage are important because early deterioration is common in the first few hours after intracranial hemorrhage onsets. More than 20% of patients will experience a decrease in the Glasgow Coma Scale (GCS) of 2 or more points between the prehospital emergency medical services (EMS) assessment and the initial evaluation in the emergency department (ED) [6]. It is critical for deciding on the need and approach for emergent surgical intervention. The surgical intervention aims to prevent herniation, reduce the intracranial pressure and reduce the pathophysiological impact of the hematoma on the surrounding tissue. This is achieved by reducing the mass effect cellular toxicity of the blood product [7]. Recognizing intracranial hemorrhage in head CT is also essential for allowing safe administration of thrombolytic therapy in acute ischemic stroke. Since “time is brain”, increased speed and reduced error in these clinical settings would constitute life-saving innovations.

Machine learning has become popular over the past few years, particularly deep learning which is a branch of machine learning that employs multi-layered neural networks. It has shown huge potential in extracting important information from medical images. Deep learning has been involved in a few medical fields which include grading of detection of metastases in histologic sections of lymph nodes [8], classification of images of skin cancer [9], and diabetic retinopathy on retinal fundus photographs[10] with high accuracies. It has proved to be accurate in image classification and processing tasks, mainly using convolutional neural networks (CNN) [11]. The same method will be implemented in the head CT scan image. It will involve image segmentation and the processed image will be trained by a deep learning approach to detect hemorrhage in the scan which is classified into cases with hemorrhage and cases without hemorrhage with great

accuracy.

Deep learning transforms the dataset by mapping them with high dimension space. For image classification, the convolutional neural network in deep learning will provide huge support with advanced techniques [12]. CNN extracts the semantic features and network-fused features of the dataset to classify the images [13]. Due to the deep nature of the network, high-resolution image classification is well supported by the convolutional neural network. This is important as most of the medical data must be in high-quality resolution to prevent missed diagnosis of diseases that could harm the patient as this will delay the management [14].

2.0 METHOD

2.1 Study Design

This was a cross-sectional study using secondary data, in which the 200 data was collected from public datasets. This dataset is owned by Abdul Kader Helwan, academic staff at Al-Manar University of Tripoli, Lebanon [15]. Permission to use the dataset for this research was officially obtained from the owner. All of the samples had been anonymized into secondary data.

The study population consisted of all adult patients who underwent head CT scan with intracranial hemorrhage and without intracranial hemorrhage from public datasets. Inclusion criteria include both gender, CT brain of all types of ICH, CT brain of normal findings, CT of ICH with a formal report which is categorized by the dataset provider. The exclusion criteria include CT brain without anonymization into secondary data, CT brain with artifacts, low-quality CT brain images which is not suitable for making a diagnosis.

The CT brain with radiological findings of intracranial hemorrhage and without intracranial hemorrhage was classified by the dataset provider. A total of 100 CT brain with hemorrhage and another 100 CT brain without hemorrhage was put in two different folders. The dataset was classified based on a formal report of the CT scan.

2.2 Sampling Method

The sampling method is simple random sampling. The units in the sampling frame were numbered from 1 to N. A series of random numbers between 1 to N were drawn by using the Table of Random Number. The units that were selected were the sample. The sample was coded with 1 for cases with intracranial hemorrhage and 0 for cases

without hemorrhage. A complete list sample of head CT scans was obtained from public datasets. The samples were chosen from the list using a simple random sampling method. All of the samples has been anonymized into secondary data. . The data is in DICOM format. All of this data is converted to PNG format. PNG format is more ready to be used and utilized by any machine learning framework [16].

For the development of the algorithm, we used a Jupyter Notebook as a platform for the training process. Jupyter Notebook is a free and open-source platform with an interactive web tool [17]. It is a web-based application where the system can run the phyton programming language. Python is the most popular language for developing an algorithm for artificial intelligence [18].

2.3 Convolutional Neural Networks (CNNs)

There are several types of deep neural networks, one of them is Convolutional Neural Networks (CNNs), which are used to build the algorithm model in this study. A CNN is a type of Feed-Forward Neural Network (FFNN) that is inspired by sophisticated biological processes [19]. It consists of many layers that can be classified into two main types: convolution layer and pooling (sub-sampling) layer. These two types of layers are alternately arranged to form a deep structure. The last layers are fully connected layers that have full connections to the previous layers, as commonly seen in traditional ANNs.

The architecture of the convolutional neural network is as shown in Figure 1. It consists of convolution layers, pooling layers, and fully connected layers. In the first layer, the convolutional filter was used to generate the convolution or feature maps of size by sliding the filter over the image and convolving it with the square input data that fits the kernel. The intracranial hemorrhage features are extracted from input images in the convolution layers. The mathematical operation of convolution preserves the spatial relationship between pixels.

The following layer is called pooling in which the dimensionality of feature maps generated in the first layer is reduced. This operation requires a selection window size from each feature map and takes the largest element from the rectified feature map within that window. Although we may take the average (Average Pooling) or sum of all elements in that selected window, taking the maximum (Max Pooling) has been more common and shown to work better [20]. The pooling operation essentially reduces the spatial dimension of input maps and allows the CNN to learn some invariance to moderate distortions in the

training; this feature enhances the generalization of the CNN at test time as the model is more tolerant to moderate distortion in the test data [21][22].

Convolution and pooling layers will be repeated many times depending on the CNN desired architecture and finally reach the final layer of the network named, The Fully Connected layer as shown in Figure 1. The features from the previous layers are forward-propagated through the network and fed into this fully connected layer with an output layer. For learning the classifier model, the conventional backpropagation learning algorithm is used to train the fully connected network and update the model parameters via gradient descent update rule [23]

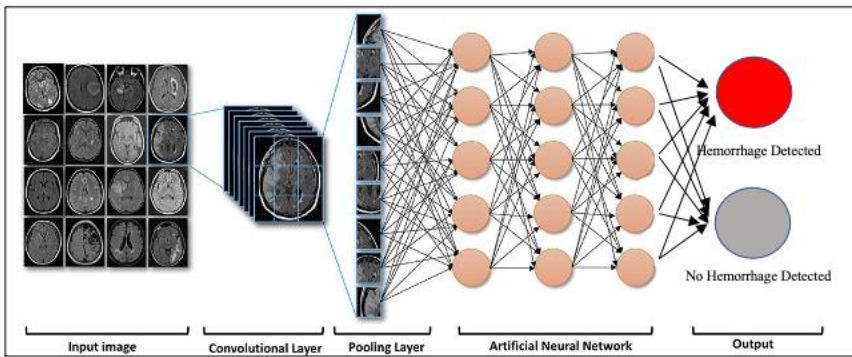


Figure 1. The Concept of Convolutional Neural Network

2.4 Data Analysis

To analyze the algorithm model performance, we used a confusion matrix to measure the accuracy, sensitivity, specificity, precision, and F1 score [24]. The confusion matrix is a matrix sized 2×2 for binary classification with actual values on one axis and predicted on another. We classified the result into a true positive, true negative, false negative, and false-positive as shown in Table 1. The true positive (TP) model correctly predicts the positive class (prediction and actual both are positive). The true negative (TN) model correctly predicts the negative class (prediction and actual both are negative). The false-positive (FP) model gives the wrong prediction of the negative class (predicted-positive, actual-negative). The false-negative (FN) model wrongly predicts the positive class (predicted-negative, actual-positive).

Table 1. Example of Confusion Matrix

| | | ACTUAL | |
|------------|----------|-------------------|-------------------|
| | | Negative | Positive |
| PREDICTION | Negative | TRUE NEGATIVE | FALSE NEGATIVE |
| | Positive | FALSE POSITIVE | TRUE POSITIVE |

From the confusion matrix, we can measure precision by calculating the percentage of true positive results as shown in Equation 1. We also can measure sensitivity and specificity based on the formula shown in Equation 2 and Equation 3. F1 score is the harmonic mean of the precision and sensitivity as shown in Equation 4. The highest possible value of an F-score is 1, indicating perfect precision and recall, and the lowest possible value is 0 if either the precision or the recall is zero.

$$Precision = TP / (TP + FP) \tag{1}$$

$$Sensitivity = TP / (TP + FN) \tag{2}$$

$$Specificity = TN / (TN + FP) \tag{3}$$

$$F1\ score = (2 * (Precision * Sensitivity)) / (Precision + Sensitivity) \tag{4}$$

3.0 RESULT

3.1 Data Pre-processing and Augmentation

First, we randomly divided our images into training and validation. A total of 200 datasets were used. We further divided it into two folders, one with head CT with hemorrhage, another folder for head CT without hemorrhage. All images will be converted from DICOM format to PNG format which is the better format to be utilized in any machine learning framework [16].

In the pre-processing step, the redundant data that are stored within CT images such as files name, dates, and so on, are manually removed to enhance the performance of classification as shown in Figure 2. Augmentation was done to enrich the information of pre-processed images. This will help pre-empt overfitting or memorization of training data and has been shown to increase the accuracy and generalization of CNNs [25]. In the augmentation step, a few techniques of rotation are used as shown in Figure 3.

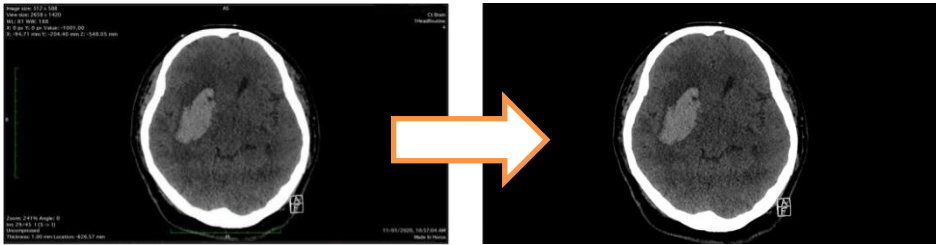


Figure 2. Removing Data from Image Sample

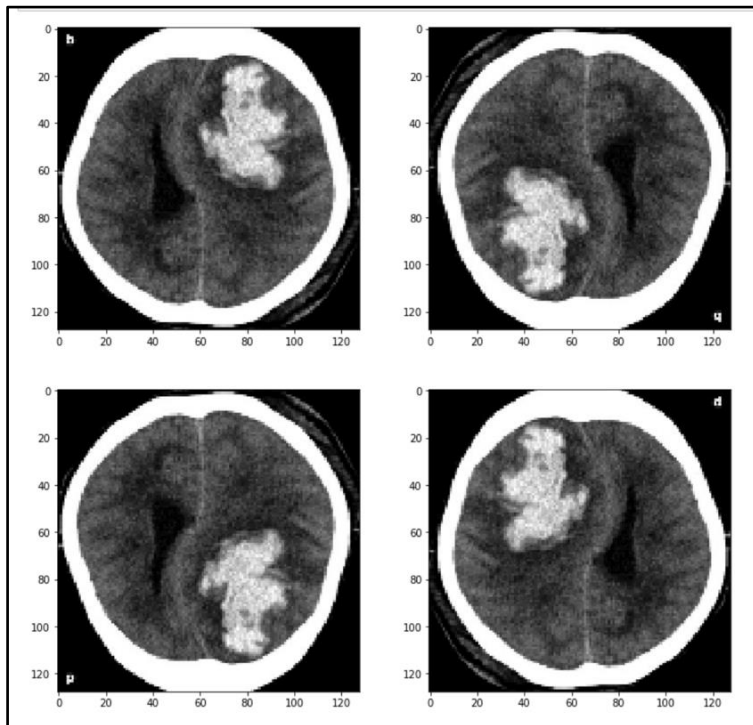


Figure 3. Data is Rotated for the Augmentation Process. Rotated images with 90,180 and 270 degrees.

3.2 Convolutional Neural Networks

Generally, a CNN relies on architectural features which include the receptive field, weight sharing, and pooling operation to take into account the 2D characteristic of structured data such as images [26]. The concept of weight sharing for convolution maps drastically reduces model parameters; this has important implications that the model is less prone to over-fitting as compared to fully connected models of comparable size.

During the training process, the loss and accuracy values are recorded and plotted as shown in Figure 4. The plot shows that accuracy increases and loss decrease over time during the training process.

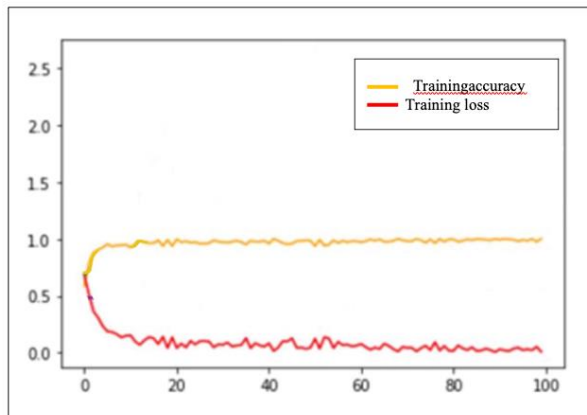


Figure 4. Loss and Accuracy Value during Training and Validation Process

3.3 Evaluating the Trained Model

Model performance is evaluated using a confusion matrix to measure the accuracy, precision, sensitivity, specificity, and F1 score. The images to validate the accuracy of the model are shown in Figure 5. Each image is then compared with the list of datasets which was categorized by dataset provider based on CT scan formal report for confirmation of the findings.

The confusion matrix derived from the model showed great performance results. From 200 training data, 95 samples showed true positive, 95 samples showed true negative, 7 samples showed false

positive, and 3 samples showed false negative as shown in Table 2. From this data, we calculated the sensitivity, specificity, precision, accuracy, and F1 score of the algorithm model. All results showed a great performance score as shown in Table 3. Figure 6 shows one of the examples of intracranial hemorrhage detection using the algorithm model we have created.

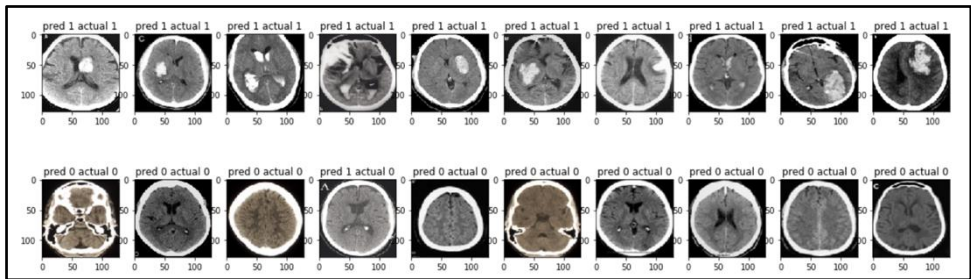


Figure 5. Images Check done during Model Development. Results of 1 = haemorrhage detected, 0 = no haemorrhage detected

Table 2. Model Confusion Matrix

| | Actual positive | Actual negative |
|--------------------|-----------------|-----------------|
| Predicted positive | 95 | 7 |
| Predicted negative | 3 | 95 |

Table 3. The calculation for Sensitivity, Specificity, Precision, Accuracy, and F1 Score derived from Confusion Matrix

| Measure | Value | Derivations |
|-------------|--------|------------------------------|
| Sensitivity | 0.9694 | $TPR = TP / (TP + FN)$ |
| Specificity | 0.9314 | $SPC = TN / (FP + TN)$ |
| Precision | 0.9314 | $PPV = TP / (TP + FP)$ |
| Accuracy | 0.9500 | $ACC = (TP + TN) / (P + N)$ |
| F1 Score | 0.9500 | $F1 = 2TP / (2TP + FP + FN)$ |

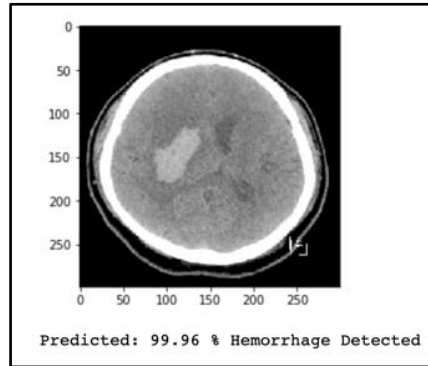


Figure 6. Result of Head CT with Intracranial Hemorrhage Detection

4.0 DISCUSSION

Intracranial hemorrhage is one of the common causes of morbidity and mortality in the world [27]. It is a medical emergency and needs to be recognized and treated urgently. Missed diagnosis of intracranial hemorrhage would harm the patient and increase mortality as well as morbidity. Study shows that the mortality rate increased up to 50% after the hemorrhage within the first 30 days [28]. Medical imaging is an important method to help in making the diagnosis of intracranial hemorrhage. The most common imaging that is used worldwide is a head CT scan. CT scan has high sensitivity and specificity in the detection of hemorrhage especially in acute stages [29].

Over the past decades, the Computer-Aided Diagnosis (CAD) system has been used as an aiding tool to help doctors in making the diagnosis of the head CT scan [30]. It has been shown to help in reducing the workload of doctors [31]. Head CT classification could be a tough task even for a radiologist. This is worst when a lot of head CT scan is involved. Hence, computer-aided diagnosis (CAD) systems have been used to extract useful information from the brain CT to help doctors in having a preliminary quantitative insight about the brain [32]. However, CAD systems can't achieve a highly significant level to make decisions on the type of medical conditions found in a brain CT scan. Thus, the CAD role was left as visualization functionality that helps doctors in making decisions.

Recently, a rapid rising in deep learning was seen. Deep learning has been applied to solve challenging problems in medical fields, such as medical image classification and analysis. It also shows great efficiency in various medical areas such as medical image analysis [33],

medical organ detection [34], disease detection [35], and many more. In some situations, those algorithms have outperformed the human medical expert's experience in diagnosis. With the help of high network performance and their 'biologically inspired' deep structure, this attracts many researchers to apply deep networks for image classification, including for brain hemorrhage CT image classification. This is because the task to detect hemorrhage could be a tedious task, even for medical experts especially for visualizing the hemorrhage in its early stages.

In this study, 200 samples were used for the training and testing of the algorithm. Deep learning using a convolutional neural network (CNN) has been employed successfully to detect brain hemorrhage. From the result of this algorithm model, intraparenchymal hemorrhages, extradural and subdural hemorrhage was detected with the highest probability. These were typically hyperattenuating and surrounded by normal tissues which make the hemorrhage more obvious compared to other types of intracranial hemorrhage such as subarachnoid hemorrhage and intraventricular hemorrhage. Almost all cases with intraparenchymal, epidural, and subdural hemorrhage gave true positive results. Only one case of subdural hemorrhage gave a false negative result. This is due to its location at the left temporal region likely due to its small size and obscured by beam hardening artifact of adjacent bones as shown in Figure 7.



Figure 7. Acute Subdural Hemorrhage at Left Temporal Region Missed Interpreted as Negative Result of Hemorrhage by Algorithm Module

The subarachnoid hemorrhage is relatively difficult to detect especially in a small amount of hemorrhage. This type of hemorrhage is typically narrow with blood filling in the sulci. In some cases, this type of hemorrhage has the same attenuation with brain parenchyma

which makes the detection even more challenging. Two cases of subarachnoid hemorrhage showed false negative results as shown in Figure 8, the same issue with intraventricular hemorrhage. One case with intraventricular hemorrhage gave false negative result. This is due to the small size and located at posterior of the occipital horn.

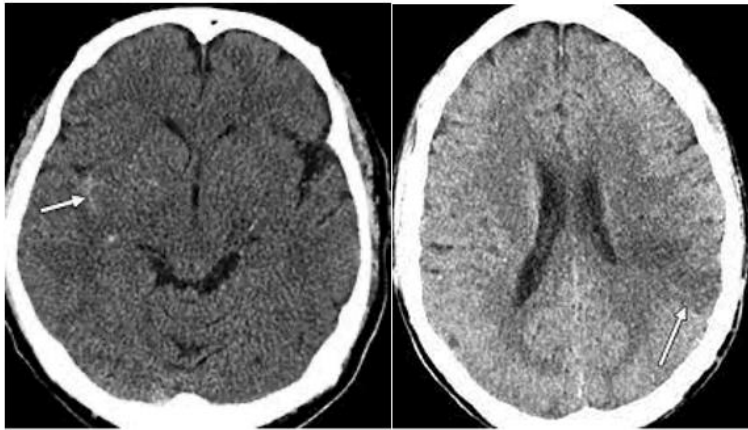


Figure 8. Acute Subarachnoid Hemorrhage (arrow) Missed Interpreted as Negative Hemorrhage by Algorithm Module

There are 7 cases that gave false-positive results. This is due to the presence of calcification in the brain parenchyma. Normal calcification usually has attenuation $>100\text{HU}$ [36]. But in some cases, the calcification can give attenuation of $50 - 100 \text{HU}$ which is the same attenuation with hemorrhage which makes it difficult to differentiate with hemorrhage as shown in Figure 9. As a radiologist, they will recognize the typical area of calcification and correlate with the patient clinical findings. This will help them to decide between calcification and hemorrhage in head CT. As for deep learning, the algorithm module will be evaluated solely on the attenuation of lesions in head CT.

The overall sensitivity of this algorithm is 95.9% which is a great achievement. But some of the cases show false-positive results which cannot be allowed in real medical practice. Moreover, this algorithm module is only able to detect acute hemorrhage. The hyperacute, subacute, and chronic hemorrhage cannot be detected using this algorithm module due to different attenuation of hemorrhage [37]. Hence, this algorithm module is just a supplementary method to help doctors in the early detection of acute intracranial hemorrhage. The need for evaluation by the radiologist is compulsory to form a final

official report of the head CT.



Figure 9. Basal Ganglia Calcification Missed Interpreted as Hemorrhage

5.0 CONCLUSION

In this study, we have successfully developed an algorithm model and proved that deep learning by using CNN enables us to create an accurate classifier that can differentiate between head CT scan with hemorrhage and without hemorrhage. The algorithm model will help to reduce the probability of missed interpretation of intracranial hemorrhage in the head CT scan. This is very crucial as missed findings of intracranial hemorrhage in the head CT caused delayed management to the patient. This will cause significant morbidity and mortality to the patient since “time is brain”, increased speed and reduced error in these clinical settings would constitute life-saving innovations.

6.0 DECLARATION OF COMPETING INTEREST

The authors declare that they have no known competing financial interests or personal relationships that could have appeared to influence the work reported in this paper.

7.0 ACKNOWLEDGMENTS

I would like to acknowledge everyone who had contributed directly or indirectly to my research accomplishment.

First and foremost, I would like to express my deepest gratitude to my research supervisor, Prof. Dr. Ahmad Bin Sobri who had given me invaluable guidance, encouragement, and continuous supervision throughout my study period. This study would not be possible without his help.

Sincere thanks also go to my research co-supervisor, Dr. Aqilah Binti Baseri Huddin for providing me advice and endless knowledge regarding artificial intelligence. Her interest in artificial intelligence had indeed inspired me.

8.0 REFERENCES

- [1] K. Blennow *et al.*, "Traumatic brain injuries," *Nature Reviews Disease Primers*, vol. 2, pp. 1–19, 2016, doi: 10.1038/nrdp.2016.84.
- [2] J. Borsch, "Ovulationshemmer oder abtreibungspille? So wirken notfallkontrazeptiva," *Deutsche Apotheker Zeitung*, vol. 153, no. 9, pp. 32–33, 2013.
- [3] A. M. Naidech, "Intracranial hemorrhage," *American Journal of Respiratory and Critical Care Medicine*, vol. 184, no. 9, pp. 998–1006, 2011, doi: 10.1164/rccm.201103-0475CI.
- [4] G. Rath and B. Ray, "Head Injury: Assessment and Early Management," *Practice Guidelines in Anesthesia*, no. January 2014, pp. 53–53, 2016, doi: 10.5005/jp/books/12644_7.
- [5] W. M. Strub, J. L. Leach, T. Tomsick, and A. Vagal, "Overnight preliminary head CT interpretations provided by residents: Locations of misidentified intracranial hemorrhage," *American Journal of Neuroradiology*, vol. 28, no. 9, pp. 1679–1682, 2007, doi: 10.3174/ajnr.A0653.
- [6] J. S. Moon *et al.*, "Prehospital neurologic deterioration in patients with intracerebral hemorrhage," *Critical Care Medicine*, vol. 36, no. 1, pp. 172–175, 2008, doi: 10.1097/01.CCM.0000297876.62464.6B.
- [7] J. C. Hemphill *et al.*, "Guidelines for the Management of Spontaneous Intracerebral Hemorrhage: A Guideline for Healthcare Professionals from the American Heart

- Association/American Stroke Association," *Stroke*, vol. 46, no. 7, pp. 2032–2060, 2015, doi: 10.1161/STR.000000000000069.
- [8] B. E. Bejnordi *et al.*, "Diagnostic assessment of deep learning algorithms for detection of lymph node metastases in women with breast cancer," *JAMA - Journal of the American Medical Association*, vol. 318, no. 22, pp. 2199–2210, 2017, doi: 10.1001/jama.2017.14585.
- [9] A. Esteva *et al.*, "Dermatologist-level classification of skin cancer with deep neural networks," *Nature*, vol. 542, no. 7639, pp. 115–118, 2017, doi: 10.1038/nature21056.
- [10] V. Gulshan *et al.*, "Development and validation of a deep learning algorithm for detection of diabetic retinopathy in retinal fundus photographs," *JAMA - Journal of the American Medical Association*, vol. 316, no. 22, pp. 2402–2410, 2016, doi: 10.1001/jama.2016.17216.
- [11] Y. Lecun, Y. Bengio, and G. Hinton, "Deep learning," *Nature*, vol. 521, no. 7553, pp. 436–444, 2015, doi: 10.1038/nature14539.
- [12] C. Tang, Q. Zhu, W. Wu, W. Huang, C. Hong, and X. Niu, "PLANET: Improved Convolutional Neural Networks with Image Enhancement for Image Classification," *Mathematical Problems in Engineering*, vol. 2020, 2020, doi: 10.1155/2020/1245924.
- [13] A. Usha Ruby, P. Theerthagiri, I. Jeena Jacob, and Y. Vamsidhar, "Binary cross entropy with deep learning technique for image classification," *International Journal of Advanced Trends in Computer Science and Engineering*, vol. 9, no. 4, pp. 5393–5397, 2020, doi: 10.30534/ijatcse/2020/175942020.
- [14] A. Pinto, "Spectrum of diagnostic errors in radiology," *World Journal of Radiology*, vol. 2, no. 10, p. 377, 2010, doi: 10.4329/wjr.v2.i10.377.
- [15] A. Helwan, G. El-Fakhri, H. Sasani, and D. Uzun Ozsahin, "Deep networks in identifying CT brain hemorrhage," *Journal of Intelligent and Fuzzy Systems*, vol. 35, no. 2, pp. 2215–2228, 2018, doi: 10.3233/JIFS-172261.
- [16] P. Lakhani, D. L. Gray, C. R. Pett, P. Nagy, and G. Shih, "Hello World Deep Learning in Medical Imaging," 2018.
- [17] А. Якимчик, "Jupyter Notebook: система интерактивных научных вычислений," 2019.
- [18] R. Browse and J. Glasgow, "Programming Artificial Languages

for," vol. 11, pp. 431–448, 1984.

- [19] M. Matsugu, K. Mori, Y. Mitari, and Y. Kaneda, "Subject independent facial expression recognition with robust face detection using a convolutional neural network," *Neural Networks*, vol. 16, no. 5–6, pp. 555–559, 2003, doi: 10.1016/S0893-6080(03)00115-1.
- [20] P. Baldi, "Autoencoders, Unsupervised Learning, and Deep Architectures," *ICML Unsupervised and Transfer Learning*, pp. 37–50, 2012, doi: 10.1561/2200000006.
- [21] K. Simonyan and A. Zisserman, "Very deep convolutional networks for large-scale image recognition," *3rd International Conference on Learning Representations, ICLR 2015 - Conference Track Proceedings*, pp. 1–14, 2015.
- [22] J. Weston, F. Ratle, and R. Collobert, "Deep learning via semi-supervised embedding," *Proceedings of the 25th International Conference on Machine Learning*, pp. 1168–1175, 2008, doi: 10.1145/1390156.1390303.
- [23] D. Erhan, A. Courville, Y. Bengio, and P. Vincent, "Why does unsupervised pre-training help deep learning?," *Journal of Machine Learning Research*, vol. 9, pp. 201–208, 2010.
- [24] D. Visa Sofia, "Confusion Matrix-based Feature Selection Sofia Visa," *ConfusionMatrix-based Feature Selection Sofia*, vol. 710, no. January, p. 8, 2011.
- [25] R. Wu, S. Yan, Y. Shan, Q. Dang, and G. Sun, "Deep Image: Scaling up Image Recognition," 2015.
- [26] T. F. Gonzalez, "Handbook of approximation algorithms and metaheuristics," *Handbook of Approximation Algorithms and Metaheuristics*, pp. 1–1432, 2007, doi: 10.1201/9781420010749.
- [27] U. Balasooriya and M. U. S. Perera, "Intelligent brain hemorrhage diagnosis using artificial neural networks," *BEIAC 2012 - 2012 IEEE Business, Engineering and Industrial Applications Colloquium*, pp. 128–133, 2012, doi: 10.1109/BEIAC.2012.6226036.
- [28] R. Badenes and F. Bilotta, "Neurocritical care for intracranial haemorrhage: A systematic review of recent studies," *British Journal of Anaesthesia*, vol. 115, no. December, pp. ii68–ii74, 2015, doi: 10.1093/bja/aev379.
- [29] F. Alobeidi and R. I. Aviv, "Basel Emergency Imaging of

- Intracerebral Haemorrhage,” *Frontiers of Neurology and Neuroscience*, vol. 37, pp. 13–26, 2015, doi: 10.1159/000437110.
- [30] J. Napier, C. J. Debono, P. Bezzina, and F. Zarb, “A CAD System for Brain Haemorrhage Detection in Head CT Scans,” *EUROCON 2019 - 18th International Conference on Smart Technologies*, pp. 1–6, 2019, doi: 10.1109/EUROCON.2019.8861833.
- [31] Q. Li and R. M. Nishikawa, “Computer-aided detection and diagnosis in medical imaging,” *Computer-Aided Detection and Diagnosis in Medical Imaging*, pp. 1–425, 2015, doi: 10.1201/b18191.
- [32] S. Yu and L. Guan, “A CAD system for the automatic detection of clustered microcalcifications in digitized mammogram films,” *IEEE Transactions on Medical Imaging*, vol. 19, no. 2, pp. 115–126, 2000, doi: 10.1109/42.836371.
- [33] D. Hutchison, “and Data Labeling,” vol. 2, pp. 21–29, 2016, doi: 10.1007/978-3-319-46976-8.
- [34] A. Helwan and D. Uzun Ozsahin, “Sliding Window Based Machine Learning System for the Left Ventricle Localization in MR Cardiac Images,” *Applied Computational Intelligence and Soft Computing*, vol. 2017, 2017, doi: 10.1155/2017/3048181.
- [35] S. Albarqouni, C. Baur, F. Achilles, V. Belagiannis, S. Demirci, and N. Navab, “AggNet: Deep Learning From Crowds for Mitosis Detection in Breast Cancer Histology Images,” *IEEE Transactions on Medical Imaging*, vol. 35, no. 5, pp. 1313–1321, 2016, doi: 10.1109/TMI.2016.2528120.
- [36] J. L. Nute, L. Le Roux, A. G. Chandler, V. Baladandayuthapani, D. Schellingerhout, and D. D. Cody, “Differentiation of low-attenuation intracranial hemorrhage and calcification using dual-energy computed tomography in a phantom system,” *Investigative Radiology*, vol. 50, no. 1, pp. 9–16, 2015, doi: 10.1097/RLI.000000000000089.
- [37] P. M. Parizel, S. Makkat, E. Van Miert, J. W. Van Goethem, L. Van den Hauwe, and A. M. De Schepper, “Intracranial hemorrhage: Principles of CT and MRI interpretation,” *European Radiology*, vol. 11, no. 9, pp. 1770–1783, 2001, doi: 10.1007/s003300000800.

THERMO-PNEUMATIC MICROPUMP FOR DRUG DELIVERY APPLICATIONS

N.A. Hamid^{1*}, B.Y. Majlis², J. Yunas² and M. Ibrahim³

¹Fakulti Kejuruteraan Elektronik dan Kejuruteraan Komputer (FKEKK),
Universiti Teknikal Malaysia Melaka, 76100 Durian Tunggal, Melaka, Malaysia.

²Institute of Microengineering and Nanoelectronics (IMEN),
Universiti Kebangsaan Malaysia, 43600, Bangi, Selangor, Malaysia

³Fakulti Teknologi Kejuruteraan (FTK),
Universiti Teknikal Malaysia Melaka, 76100 Durian Tunggal, Melaka, Malaysia.

*Corresponding Author's Email: norihan.hamid@utem.edu.my

Article History: Received December 18, 2021; Revised January 23, 2022;
Accepted January 25, 2022

ABSTRACT: Micropumps constitute an essential part of precise delivery and directional volume control of fluid in a microfluidic system. In biomedical applications, micropump is widely used especially in drug delivery, biological fluid transmission, organic analysis, liquid measurement, and many more. In this paper, the concept and design structure hence fabrication of the Thermo pneumatic micropump prototype are explained. The experimental measurement of the micropump employing planar diffuser nozzle in transmits fluid is also presented. Thermopneumatic micropump is comprised of three different components which are the microheater on the bottom, the flexible thin membrane that acts as an actuator, and the planar diffuser nozzle on the top to channel the fluidic. These three components were fabricated separately due to the different materials and techniques used in each component. Finally, the whole micropump system was integrated using an anodic bonding technique. Bulk micromachining technique was used to fabricated the chamber and thin-film membrane, surface micromachining technique for the microheater while replica molding technique was used for the planar diffuser nozzle. The whole diameter size for the micropump was 25 x 20 x 1.6 mm respectively. The microscope image recorded video and data was used during the experimental measurement, to observed and calculate the flow rate of meniscus motion flow in the outlet tube of the micropump. At the end of the experiment, the flow rate range of the micropump measure was

approximately 770pL to 12.5nL, when the output of 2-12Vdc was applied to the microheater. This flow rate range is very suitable for drug delivery applications.

KEYWORDS: *Thermo-pneumatic, micropump, drug delivery, thin-film membrane*

1.0 INTRODUCTION

The emergence of MEMS microdevices has been pioneered in various fields over the decade. The new application of MEMS devices is being discovered continuously. Presently, MEMS technology and microdevice have embarked and been emphasized in the medical field including drug delivery and development, point of care diagnostic, sensitive bioanalytical systems, surgical and therapeutic microsystems. [1-3]. These microdevices have placed importance on the technology in providing a better outcome for the patient and a lower overall health care cost [4-5].

MEMS micropump has played a crucial role in controlling drug delivery to a specific target in these few years. Compare with the traditional oral and manual injection for therapeutic effect, consumption of micropump in drug delivery system is higher reliable and efficient [6-7]. Besides, micropumps offer precise dosage, continuously and automated delivery approach pharmaceutical therapy treatment [8-9]

This paper provides an explanation of thermo pneumatic micropump from the beginning of fabrication until the flowrate measurement for the completed micropump system. Three fabrication techniques have been described for the three-part of a micropump component such as bulk micromachining technique of microactuator membrane and chamber, surface micromachining technique for the microheater, and replica molding for the planar diffuser nozzle channel. Before that, the micropump's brief concept and structure were also presented. Next, the experimental setup for the flowrate measurement was explained in detail. At the end of the experiment, the measurement of flow rate is performed in a graph chart and a point of discussion is also provided.

2.0 CONCEPT AND STRUCTURE

Thermo pneumatic micropump uses the concept thermal expansion method which involves the volume expansion or induces stress of material in response to change in temperature or heat convection as can be seen in Figure 1. Based on thermally induced volume change or phase change of fluid that occurred in a chamber, periodically change in volume of chamber results a pressure change inside the cavity to actuate membrane. Liquid pressure change can be expressed as:

$$\Delta P = E \left(\beta \Delta T - \frac{\Delta V}{V} \right) \tag{1}$$

where ΔP is a pressure change, E the bulk modulus of elastic, β the volume coefficient thermal expansion, ΔT the temperature increase and $\frac{\Delta V}{V}$ is the volume change percentage body [10].

In summary, membrane deflection is directly proportional to the change of temperature inside the chamber. This is also due to the elastic material properties of the membrane which can be expanded when heated. Therefore, when the microheater heats up, air space inside the microchamber will expand. At this point, volume expansion will cause the membrane to deflect and fluid was sucked into to pump. The fluid will pump out from the chamber when the heaters are cooling down.

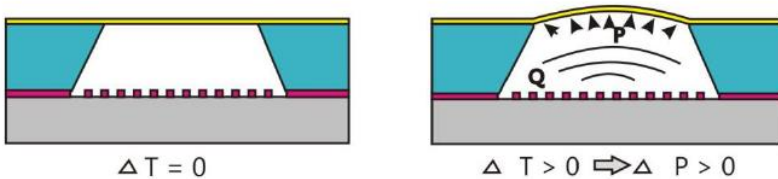


Figure 1: Concept of thermal expansion that produces pressure on the thin-film membrane when heated by the microheater.

2.1 Thermo pneumatic micropump structure

Thermo pneumatic micropump was constructed from microheater as the air supply for the pump thin-film membrane act as an actuator complete with microchamber heater as well as microchannel for fluid flow. The microheater was the main supply for the Thermo pneumatic micropump. The thin-film membrane was acted as an actuator to attract and push the fluid into the chamber while the fluid chamber is the component used during the fluid pumping process. The trapped volume air in the microchamber will be heated when the microheater

receivers the power supply hence planar diffuser nozzle was channeling the fluid flow or to control the fluid movement.

Figure 2. represents a side view of the micropump consisting of three layers of the substrate structure. The first layer is the substrate for the microheater, followed by a thin film membrane with a heating chamber on the second layer and the final layer of the planar diffuser nozzle element. The overall dimension of the pump is approximately 25 x 20 x 1.6 mm. A three-dimensional image of the micropump is depicted in Figure 3. Each pump component is fabricated separately due to the different processes and materials used. After the functionality and measurement testing for each component is completed, all components are combined using anodic bonding.

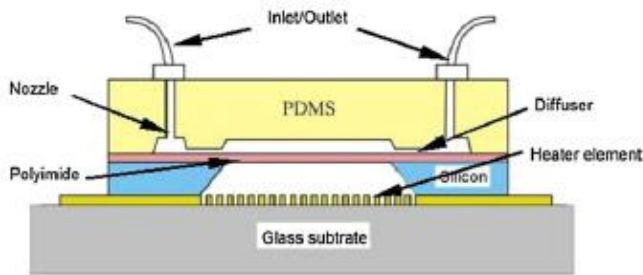


Figure 2: Side view of Thermo pneumatic micropump

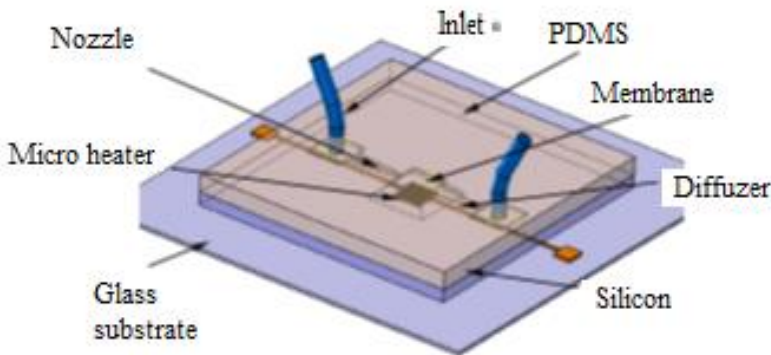


Figure 3: 3-dimensional view Thermo pneumatic micropump

Micro heater structure consists of thin-film metal elements that are deposited on a silica boron glass substrate. Besides good thermal insulation, silica boron glass is also transparent thus having the advantage to facilitate the process of aligning the entire component at

the end of the fabrication process later. The micro heating element can generate thermal energy to expand the air volume in the heating chamber and turn to deflect the thin film membrane that acts as a microactuator on the Thermo pneumatic micropump system. When this condition occurs, the pressure difference between the inlet, chamber, and outlet will allow fluid to flow in and out of the pump [11,12].

The heating chamber and flow chamber structure are designed separately to prevent the contamination of the fluid that is pumped in and out of the micropump. Normally, when heating occurs heater is concerned to produce dust or particles that can change the structure of fluid therefore by separating the design, contamination can be avoided. Thermo pneumatic micropump also choose planar diffuser nozzle because of the capability to produce a high flow rate [13,14] reduce clogging [15, 16] with low cost and ease fabrication process [17,18]

3.0 DEVICE FABRICATION

Thermo pneumatic micropump are separated into three different components which are micro heater fabrication, the diaphragm of the thin-film membrane with heater chamber fabrication, and planar diffuser nozzle fabrication. Each of these components has an essential function in the micropump system. The micropump involve three separation process due to different material and technique used. Micro heater and membrane with heater chamber fabrication used to bulk and surface micromachining technique while the planar diffuser nozzle was fabricated using mold replication technique.

3.1 Micro heater fabrication

Figure 4 represents the fabrication step of the microheater system. Firstly, a thick 180 μ m boron silica glass substrate was cleaned using RCA standard procedure to clean any grease or impurities on the glass surface. Then, the glass is baked in a hot place at 120 $^{\circ}$ C for 20 minutes for hydrophilic treatment purposes. Next, the glass is coated with a 12 μ m photoresist and pattern transfer is performed through the photolithography process. The AZ 400K developer with a ratio of 1:2 was used to develop the pattern. After drying the pattern, a metal sputtering machine was used to deposit 50 μ m chromium as an adhesive layer and 200 μ m of platinum as a conductive layer on the glass substrate. Finally, the lift-off method is performed to reveal the heater conductive element structure.

3.2 Micro actuator fabrication

A 680 μm thick <100> silicon nitride Si₃N₄ was used for a base substrate of the thin film membrane and microchamber. After the standard RCA cleaning process was completed, AZ 4620 photoresist was spun onto both sides of the nitride surface. The photoresist on the backside of nitride is thicker than the other side due to the diaphragm requirement for the next process. Then the sample was placed on the hotplate for the pre-baking step at approximately 3 min at 120°C. Then, the process was followed by pattern transfer also known as photolithography. A buffered oxide etch (BOE) solution was used to remove the exposed nitride while the unexposed nitride layer is used as a mask for potassium hydroxide (KOH) etching. Next, KOH with the concentration of 45 wt% at 80°C was applied to remove the undesired silicon layer until 100 μm thick membrane was left. At this point, polyimide was deposited on the backside of the other wafer. The polyimide needs to be cured with incremental degradation temperature from 50 – 350°C for 1 hour. The sample was then re-immersed in 35wt% KOH solution at 70°C to etch the rest of the residual silicon layer. At this point, careful observation was required to avoid the membrane tearing or damage due to the very thin layer etched. The etching was stopped after the polyimide membrane layer reveal. Until here the thin microchamber was completely performed. All of these process and step is presented in Figure 5.

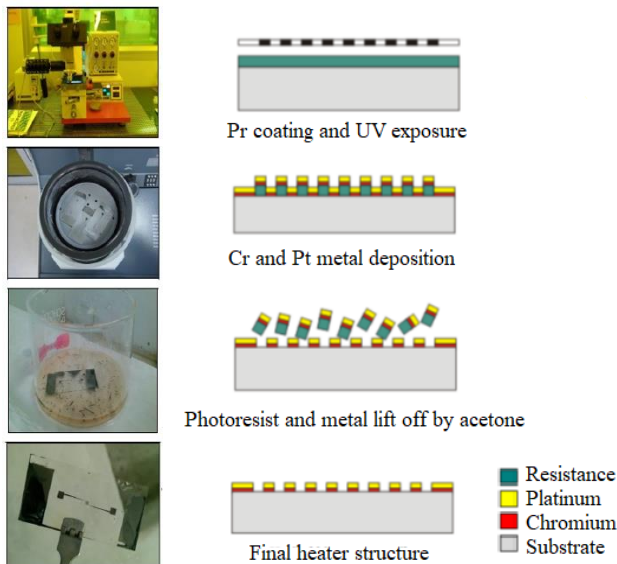


Figure 4: Fabrication steps for microheater

3.3 Diffuser nozzle fabrication

In order to construct a planar diffuser nozzle, the mold master structure must first be constructed. Same as the previous process, silicon dice must be cleaned using the RCA standard procedure before proceed to the next steps. SU8 2075 was then poured on the silicon substrate and spun on the spin coater at 500 rpm followed by 2000 rpm to get the thickness of 110 μm . Next, a photolithography process was performed to transfer the diffuser nozzle pattern. The process was then followed by the pre-baked and post-baked technique before the mold was revealed by the SU8 developer and Isopropanol (IPA). Finally, the hard mold master structure of the planar diffuser nozzle was obtained.

As shown in Figure 6, the PDMS mixture was then poured on into the SU8 mold master structure. Before that the 2 cm Tygon tube was attached to the master mold. Next, the sonification process was performed to cure the PDMS replica. The cured PDMS replicas were then peeled off from the SU8 master pattern and combined with the previous component to represent a thermopneumatic micropump system. The diffuser nozzle was fabricated with the dimension of 20 mm² at the inlet and outlet pumping chamber, 110 μm depth and 20 mm of total length with divergence angle id 10°.

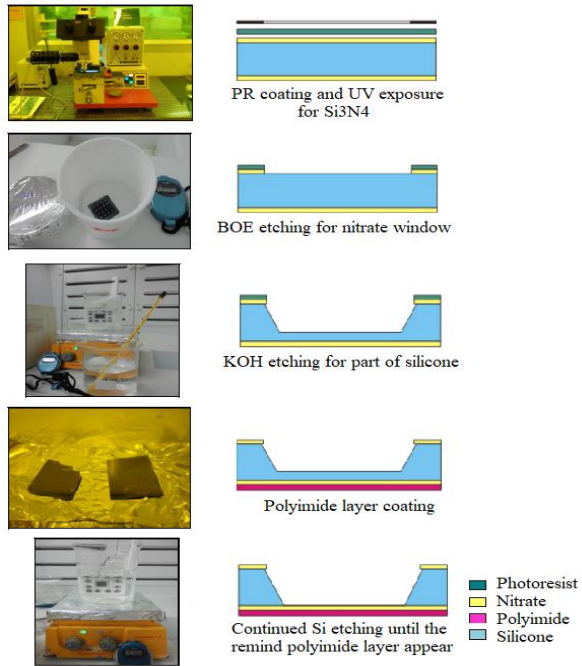


Figure 5: Fabrication steps for the microactuator

Overall, the thermo pneumatic micropump constructed consisted of a microheater, thin-film membrane with a heater chamber and planar diffuser nozzle. The microheater is built with platinum as a conductive heating element which is deposited onto boron silica glass surfaces using the surface micromachining technique. An adhesive agent between platinum and glass was 50 μm deposited chromium. Thin membrane polyimide is constructed with silicon microchamber using bulk micromachining technique act as the microactuator while the microchannel or diffuser nozzle element was fabricated from PDMS using soft lithography or replica molding technique. The whole specification of the thermopneumatic micropump can be referred on Table 1 while the actual thermo pneumatic micropump is illustrated in Figure 7.

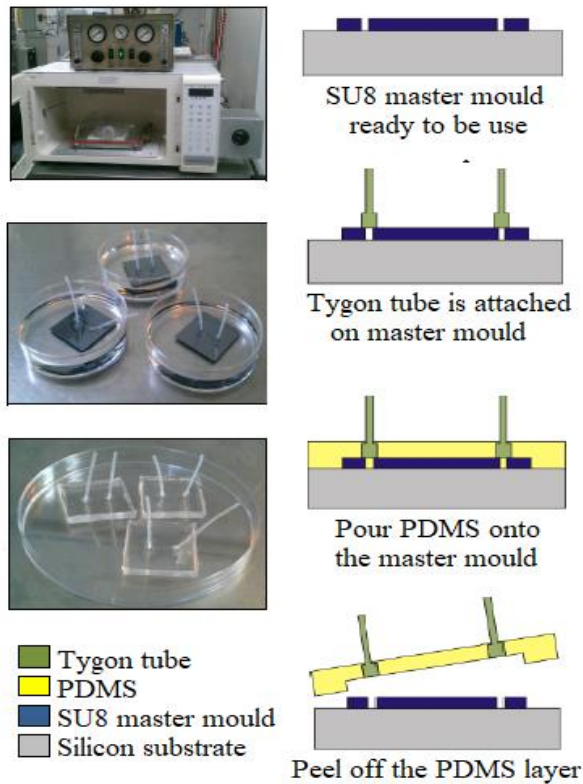


Figure 6: Fabrication steps for planar diffuser nozzle

Table 1: Specification of thermo-pneumatic micropump

| Parameters | Material | Unit |
|--------------------------------|----------|-------------------|
| Micro Heater | | |
| Width | Pt, Cr | 50 μm |
| Spaces | w | 50 nm |
| Thickness (Pt, Cr) | s | 200, 50 nm |
| Total length | t | 20 mm |
| Thin Film Membrane | | |
| Thickness | l | 4 μm |
| Area | Pi | 4 mm |
| Micro Chamber | | |
| Depth | h | 680 μm |
| Window Area | A | 20 mm |
| Trench | pole | 54.7° |
| Diffuser/nozzle element | | |
| Depth | h | 110 μm |
| Total length | l | 40 mm |

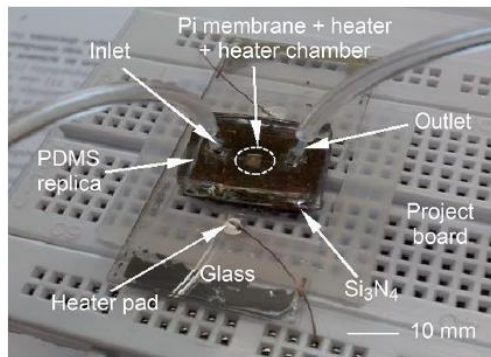


Figure 7: Actual thermopneumatic micropump

4.0 MEASUREMENT AND TESTING

After the measurement and functionally testing for each component is carried out, these three component is then integrated into one complete system using an anodic bonding technique and the whole system namely as thermopneumatic micropump. The functionality, performance, and capability of the micropump to pump the fluid were carried out as mentioned in the next paragraph.

4.1 Experimental setup

Figure 8 shows a schematic diagram and layout of a functionality test

of a thermo pneumatic micropump in the laboratory. The actual measurement is also illustrated in Figure 9. The Aigo scope image 9.0 microscope was used to record the fluid flow rate during the test. The microscope lens was placed aligned with the measurement scale and a Tygon tube. Colored ionized water was used as the fluid in the test to provide a clear observation and analysis. Next, the power supply is connected to the microheater using a wire connection on the mini-project board and a connector pad of the microheater.

When the supply is applied to the microheater, the color liquid slowly enters the diffuser inlet into the fluid chamber and then exits again at the outlet nozzle. This meniscus movement was captured and recorded for further flow rate measurement and calculation.

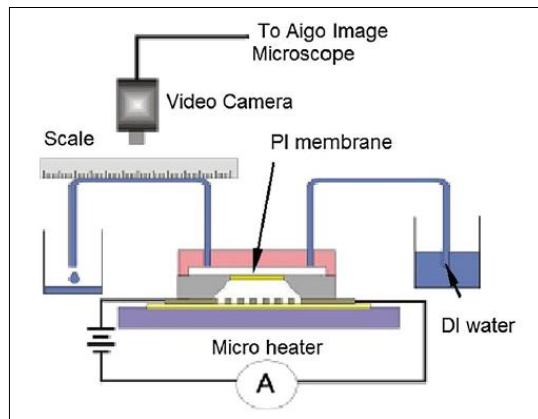


Figure 8: Schematic diagram and layout for thermo pneumatic micropump functionality test



Figure 9: Actual functionality test of thermo pneumatic micropump

5.0 RESULTS AND DISCUSSION

Figure 10 shows the recorded and captured movement of fluid from the experimental test. An initial scale of fluid before any movement is marked with the yellow line as well a reading scale is set in every 30 seconds with a scale size of 0.1 mm. The flow rate produced from the fluid motion can be determined by calculating the liquid flow along the Tygon tube with volume count in the cylinder. The meniscus transition distance fluid in this figure is taken for 2 minutes 30 seconds with the maximum input voltage of 12V.

Finally, the result of voltage supply versus flow rated is recorded in Figure 11. As shown in this figure, the pumping rate of the micropump is 770pL at a 6V input supply with 33.5°C estimation temperature in the microchamber, while the maximum flowrate is 12.5nL, 12 V and 63.5°C respectively. According to the previous functionality test on the thin film membrane and microchamber, this is the final point where the experimental test should be terminated. If the temperature inside the chamber exceeds 70°C, the thin film membrane will be torn and damaged which means all the micropump systems will also collapse.

From the experiment, it can be observed that when the power supplied increases, significantly the temperature inside the microheater will increase and the pumping rate also increase respectively. Based on previous findings in [19], the deflection of the corrugated diaphragm is about three times compared with the flat one. However, since the paper used the same concept of air expansion and cooling in the chamber cavity, both flowrate obtained can be used for the drug delivery system. As mentioned in [20], micro-dosing through drug delivery application devices requires an extremely small flow rate but there is no specific flow rate for each microdosing. There is various flowrate that has been done by the previous researcher which in as smaller 0.13 μL as and higher as 4800 μL . The flow rate range depends strongly on application. As mentioned in [20], the achieved flow between 0.77 nL/min and 12.5nL/min in this paper is suitable for micro-dosing the animal trials on small lab animals. The main concern for the drug delivery system was the safety application hence a crucial for them to have an accurate and precise flow rate. Therefore, in each design of the drug delivery system, the ability and capability of the system must be known to identify where are suitable applications can be consumed.

The material used to fabricate the components are relatively economic, easy to obtained and fabricate. Nevertheless, the consumption of supply below 12V provides a distinct advantage because it is portable and easy to obtain.

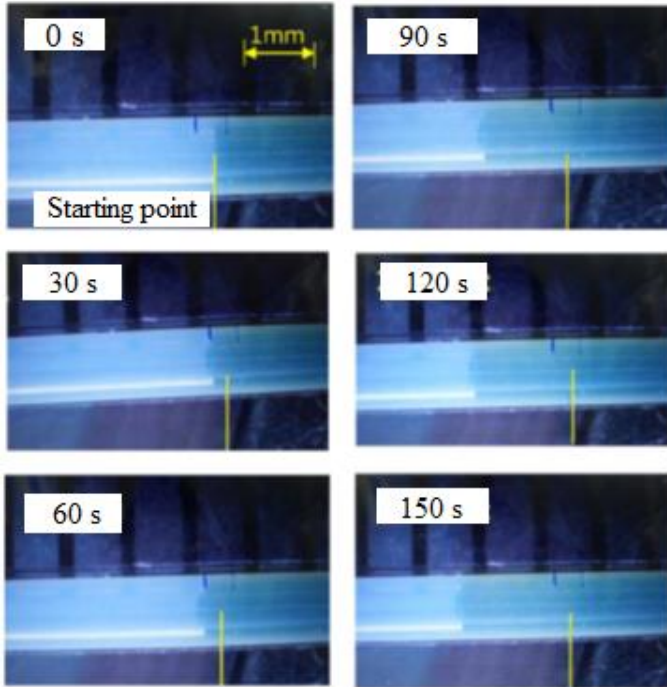


Figure 10: Distance of fluid motion for 2 min 30 second

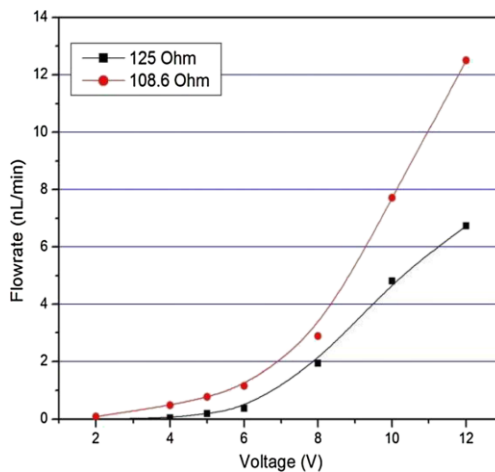


Figure 11: Relationship between flow rate and applied voltage.

6.0 CONCLUSION

In this paper, a thermo pneumatic micropump was successfully fabricated using three different processes and materials. Material, technique, dimension, and component used are explained in detail. The three components were then integrated using an anodic bonding technique to be complete the micropump system. Next, the functionality tests and flow rate measurement for the micropump are performed to determine the suitable application of the micropump in the medical field based on performance and medical device requirements. The experimental results show that with the pumping rate of 770pL-220nL, the term pneumatic system is suitable to be used as a therapeutic substances device in a drug delivery system.

7.0 ACKNOWLEDGMENTS

Authors would like thanks to Fakulti Kejuruteraan Elektronik and Kejuruteraan Komputer (FKEKK), Universiti Teknikal Malaysia Melaka for sponsoring the study. This research is also support by MEMS Group in Institute of Microelectronic and Naonatechnology (IMEN), Universiti Kebangsaan Malayisa under Arus Perdana Grant UKM.

8.0 REFERENCES

- [1] J.S. Kochhar S. Y. Chan, P. S. Ong, W. G. Lee, L. Kang, *Microfluidic Devices for Biomedical Applications*, Woodhead Publishing Series, 2013, pp.231-280
- [2] Dennis L. Polla, Arthur G. Erdman, William P. Robbins, David T. Markus, Jorge Diaz-Diaz, Raed Rizq, Yunwoo Nam, and Hui Tao Brickner, "Microdevices in Medicine", *Annual Review of Biomedical Engineering*, 2000, Vol. 2, pp. 551-576
- [3] B. Bhattacharyya, "Electrochemical Micromachining for Nanofabrication, MEMS and Nanotechnology", William Andrew Publication, 2015
- [4] M. W. Ashraf, S. Tayyab, N. Afzulpurkar, "Micro Electromechanical Systems (MEMS) Based Microfluidic Devices for Biomedical Applications", 2011, *Int. J. Molecular Sciences*, Vol. 12 (6), pp. 3648-3704.
- [5] Yao-Nan Wanga, Lung-Ming Fu, Yao-Nan Wanga, Lung-Ming

- Fu, "Micropumps and biomedical applications – A review", *J. Microelectronic Eng*, 2008, Vol. 195, pp. 121-138
- [6] N. M. Elman and U. M. Upadhyay, "Medical Applications of Implantable Drug Delivery Microdevices Based on MEMS (Micro-Electro-Mechanical-Systems)", *J. of Current Pharmaceutical Biotechnology*, 2010, Vol. 11, pp. 398-404
- [7] Faranak Rajab, Alireza Bakhshi, Ghazale Kazemi, "Drug delivery applications of mechanical micropumps," J Conference: International Conference on Applied Researches in Science & EngineeringAt: Amsterdam, Netherlands. Jan 2021, pp. 1-18.
- [8] Agnes Bußmann, Henry Leistner, Doris Zhou, Martin Wackerle 1, Yücel Congar, Martin Richter, "Piezoelectric Silicon Micropump for Drug Delivery Applications", *J. Applied Sci.* Vol. 11, 2021, pp1-14.
- [9] Farid Amirouche, Yu Zhou & Tom Johson "Current micropump technologies and their biomedical application", *J. Microsystem technologies*, 2009, Vol.15, pp. 647-666.
- [10] D. I. Brian and V. G. Surech "Recent Advances in microscale pumping technologies: a review and evaluation Microfluidic Nanofluidic", 2008, Vol. 5. pp.145-174.
- [11] S. R. Hwang, W. Y. Sim, D. H. Jeon, G. Y. Kim, S. S. Yang, & J. J. Park, (2005). "Fabrication and test of a sub microliter level thermopneumatic micropump for transdermal drug delivery", 3rd IEEE/EMBS Special Topic Conference on Microtechnology in Medicine and Biology, 2004, pp. 143–145.
- [12] S. Zimmermann, J. A. F. D. Liepmann & A. P. Pismo, "A Planar Micropump Utilizing Thermopneumatic Actuation and In-plane Flap Valves", 17th IEEE International Conference on Micro Electro Mechanical Systems (MEMS), Sep 2004, pp. 462–465.
- [13] Manoj Pandey and P.C. Upadhyay, (2012), "Design and Simulation of Valve Less PZT Micropump for Drug Delivery System". *Int. Journal of Advancement Technology*, Vol. 3, Issue 2 pp. 92-100
- [14] Stemme, G., & Stemme, E. (1993). A valveless diffuser with no nozzle-based pump. *Sensor and Actuators A*, 2(39), pp. 156–167
- [15] A. E. Guber, M. Hecke, D., Herrmann, A., Muslija, V. Saile, L. Eichhorn, G., Knebel. (2004). *Microfluidic lab-on-a-chip systems*

based on polymers – fabrication and application. *Chemical Engineering Journal*, 2004, Vo. 101, pp .447–453.

- [16] Iverson, B. D., & Garimella, S. V. (2008). Recent Advances in Microscale Pumping Technologies: A Review and Evaluation and evaluation. *Microfluidics and Nanofluidics*, Vol. 5, pp. 145–174.
- [17] Nguyen, N.-T., & Truong, T.-Q. (2004). A fully polymeric micropump based on laminar technology. *Journal of Micromechanics and Microengineering*. Vol. 14, Issue 4, pp. 632-638.
- [18] Dau, V. T., Dinh, T. X., Tanaka, K., & Sugiyama, S. (2009). Study on the geometry of valveless-micropump. 2009 IEEE/ASME International Conference on Advanced Intelligent Mechatronics, pp. 308–313.
- [19] Jeong, O. C., & Yang, S. S. (2000). Fabrication and test of a thermopneumatic micropump with a corrugated p+ diaphragm. *Sensors and Actuators A: Physical*, 83(1-3), pp.249–255.
- [20] Agnes B. B, Lorenz M. G, Claudia P. D, Thomas A. T, Axel W, Martin Richtera. (2021) “Microdosing for drug delivery application—A review”, *Sensor and Actuators A*, , Vol. 330, pp. 1-26

SMART HEALTH MONITORING SYSTEM UTILIZING INTERNET OF THINGS (IoT) AND ARDUINO

Ameyshafida Mihat¹, Norhashimah Mohd Saad^{1,*}, Ezreen Farina Shair², Rohana Abdul Rahim³ and Achmad Bayhaqi Nasir Aslam⁴

¹Fakulti Teknologi Kejuruteraan Elektrik Dan Elektronik, Universiti Teknikal Malaysia Melaka (UTeM), Jalan Hang Tuah Jaya, 76100, Durian Tunggal, Melaka, Malaysia.

²Fakulti Kejuruteraan Elektrik, Universiti Teknikal Malaysia Melaka (UTeM), Jalan Hang Tuah Jaya, 76100, Durian Tunggal, Melaka, Malaysia.

³Hospital Seri Manjung, Jalan Gapis, 32040 Seri Manjung, Perak, Malaysia

⁴Radiology Department, Medical Faculty of Universitas Brawijaya - Saiful Anwar Hospital, Jl. J. A Suprpto No 2 Malang, Indonesia.

*Corresponding Author's Email: norhashimah@utem.edu.my

Article History: Received January 9, 2022; Revised January 24, 2022;
Accepted January 24, 2022

ABSTRACT: The use of healthcare monitoring systems in hospitals and other health facilities has grown exponentially, and portable healthcare monitoring systems based on new technologies have emerged as a severe concern in several countries throughout the globe. The emergence of the Internet of Things (IoT) technology has contributed to the progress of healthcare from face-to-face counseling to telemedicine. The project aims to design a reliable health monitoring system utilizing the IoT, Arduino, and Android applications. It can be used to measure body temperature, heart rate, and level of oxygen in the blood in both hospitals and homes. The system is also capable to verify that the transmission of the sensor's data to the host computer is done in real-time. The results show that the system reading is approximately 100% accurate as of the purchased measuring instruments or actual devices. Therefore, doctors and family members can now monitor and track the patient's health anywhere through this smart health monitoring system.

KEYWORDS: *IoT, Body Temperature, Heart Rate, Blood's Oxygen Level.*

1.0 INTRODUCTION

The Internet of Things (IoT) has connected everything inside during the previous decade, and it has been labeled the next technological revolution [1]. The Internet of Things is most widely used in healthcare management, where it is used to monitor health and environmental factors. The Internet of Things (IoT) is the process of establishing a connection between computers and the internet using sensors and networks. These interlinked components might be utilized in health surveillance systems. Modern technologies now include a customizable interface, personal assistant gadgets, and mental health care to aid individuals in living more intelligent lives [2].

Health monitoring is a significant concern in today's climate. Patients have serious health difficulties as a consequence of an insufficient health monitoring system. The new health monitoring system is unable to deliver real-time patient health warnings and is constrained by the distance between the patient and the hospital [3]. Additionally, it requires time to collect data from patients. It is inefficient in terms of cost. A low-cost contemporary gadget capable of providing real-time data. The primary reason for developing this system is to address the absence of effective health monitoring in community life, the disparity between rural and urban health care centers, and the inability of the present health monitoring system to give real-time patient health alerts [4].

As a result, the usage of in hospitals and other health institutions, healthcare monitoring systems has significantly enlarged, and new technology-enabled portable healthcare monitoring devices have become a serious issue in several nations worldwide [5]. The emergence of the Internet of Things (IoT) technology has contributed to the progress of healthcare from face-to-face counseling to telemedicine. Numerous Internet of Things (IoT) applications are also being developed at the moment.

Thus, doctors and family members may now monitor or follow a patient's health using the Android application [6]. When monitoring, recording, and tracking changes in patient health metrics over time becomes necessary, Internet of Things (IoT) Monitoring comes in helpful [7]. This database of health parameter changes was created using Internet of Things (IoT) health monitoring. This article presents a smart health monitoring system that can monitor patients' fundamental health symptoms in an Internet of Things (IoT)

environment [8]. This device may be used in both hospitals and households to monitor and record numerous factors such as body temperature and heart rate [9]. This is a large sensor-based project using cutting-edge technologies.

The project aims to create a prototype of a healthcare monitoring device that can detect and wirelessly transmit a human body's temperature, pulse rate, and the level of oxygen in the blood to a host PC. The health-monitoring equipment created here is an Internet-of-Things (IoT) system. It's based on the Arduino UNO. The Arduino UNO is a common prototyping board that is often used in Internet of Things projects. To develop this medical IoT system, the Arduino is utilized to link the pulse LM-35 temperature sensor, MAX30100 pulse oximeter, character LCD, and ESP8266 Wi-Fi modem. The computed pulse rate, temperature, and oxygen saturation level in the blood are shown on the character LCD attached to an Arduino and sent to the cloud platform through a Wi-Fi access point. Regularly, health-related data such as pulse rate, body temperature, and blood oxygen saturation level are updated and recorded to the ThingSpeak platform. The data may be utilized to maintain a patient's medical history.

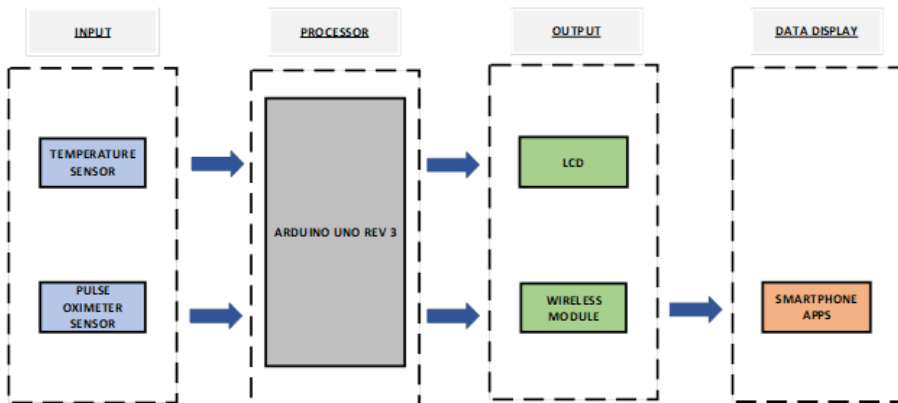


Figure 1: Smart Health Monitoring System Block Diagram

Based on Figure 1, this smart health monitoring system's inputs include a temperature sensor and a pulse oximeter sensor, which detects all of the health indicators that must be monitored. The inputs then communicate the measured parameters to the Arduino UNO, which interacts with the data and then exports it to the outputs. LCD and wireless modules serve as outputs. All parameter data is shown in the smartphone application, ThingSpeak Apps, which enables users to monitor their health status based on the gathered data.

2.0 METHODOLOGY

2.1 Hardware Design

For this Smart Health Monitoring System, based on Figure 2, the flowchart displays the whole process of constructing a project system, which includes both hardware and software required to operate the system. The system is initiated when two distinct input signals initialize the body temperature through an LM35, the heart rate through a pulse sensor, and the blood oxygen saturation level through a Max30100 pulse oximeter sensor.

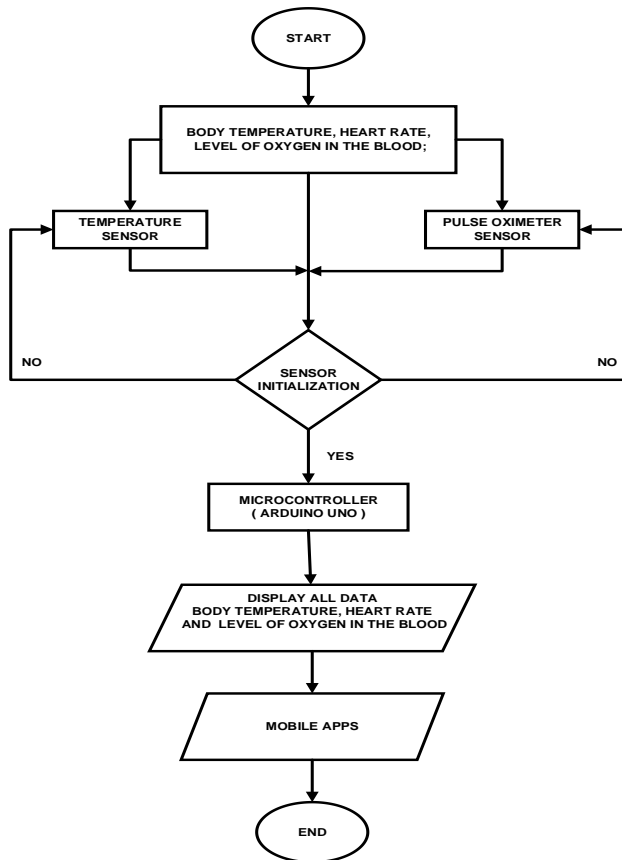


Figure 2: Overall flowchart of project system

Following successful initialization of the input sensor, both input sensors are sent to the microcontroller, which is an Arduino Uno Rev 3. After transferring the input data to the microcontroller (Arduino Uno Rev 3), the Arduino Uno rev 3 will transmit the body temperature, heart rate, and oxygen saturation level in the blood to the LCD as

output, which will be shown on the LCD screen as an output display. The data is sent in real-time to the WiFi module and then to the mobile application (www.thingspeak.com) for analysis and display. Simultaneous real-time updates of the processed and visible data represent the state of the human body's temperature, heart rate, and blood oxygen saturation level.

The schematic circuit was installed using Proteus software as shown in Figure 3. The Arduino Uno Rev 3 microprocessor acts as the microprocessor in this system that interfaces with all component input and output. These components include an LM35 and MAX30100 Pulse Oximeter sensor. The LM35 sensor is used for body temperature detection and a MAX30100 Pulse Oximeter sensor for heart rate and blood's oxygen level detection. It is located on the MAX30100 Pulse Oximeter board in the schematic as the gauge's initialization point. The body temperature, heart rate, and blood oxygen level are sensed when the fingertips are put on the MAX30100 Pulse Oximeter sensor board. The chip receives the collected data. The heart rate, blood oxygen saturation level, and temperature of the human body are all detected and shown on an LCD screen.

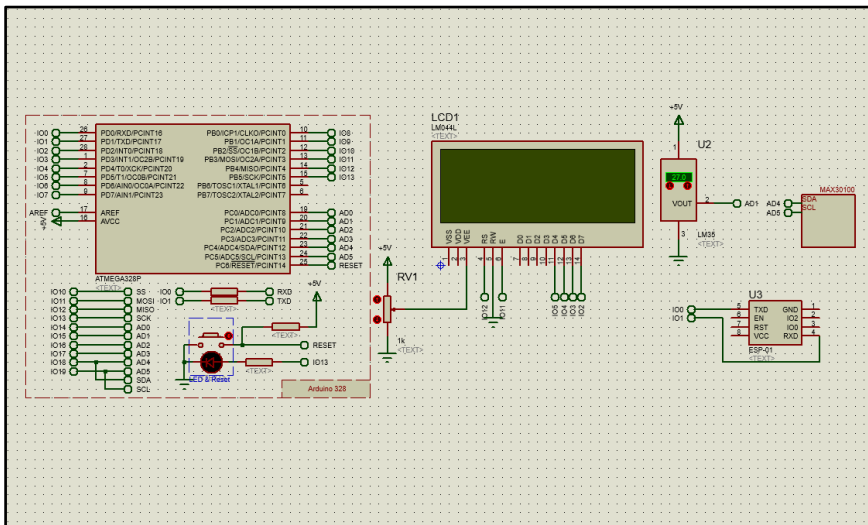


Figure 3: The architecture of a body temperature, heart rate, and blood's oxygen level system is shown schematically.

Based on Figure 4, this Arduino UNO serves as the system's brain in this project. It connects all of the input and output components. It is capable of reading inputs such as a pulse sensor, an LM-35 temperature sensor, and a biosensor and converting them to outputs such as an LCD and the ThingSpeak platform on a mobile phone.

any one moment. Our LCD has a total of 16 pins.



Figure 7: LCD 20X4 Display

NodeMCU as shown in Figure 8 is an open-source development board and firmware. It allows you to program the ESP8266 WiFi module using the Arduino IDE or the simple and powerful LUA programming language. It combines the functions of a WIFI access point and a microcontroller-based station.

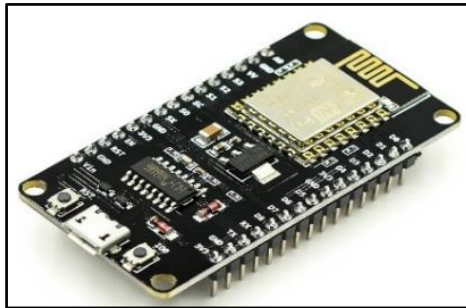


Figure 8: NodeMCU V3 ESP8266 (Wifi Module)

2.2 Software Design

This project utilizes a separate Arduino IDE (Integrated Development Environment) for software development. The Arduino IDE as shown in Figure 9 is a free and open-source software development environment for creating and compiling code for Arduino Modules. It is the official Arduino program that simplifies the learning process for non-technical individuals.



Figure 9: Integrated Development Environment (Arduino IDE)

Proteus Design Suite 8.9 as shown in Figure 10 is used to develop drawings and validate the traceability of project systems. The Proteus Design Suite is a collection of proprietary software tools used mostly for electrical design automation. Electronic design professionals and technicians create electronic schematics and print them for the production of printed circuit boards by using the Proteus software.



Figure 10: Proteus Design Suite 8.9 Version

Figure 11 shows the Overview of ThingSpeak. ThingSpeak is an open-source Internet of Things platform that enables the storage and retrieval of data from HTTP-enabled devices. ThingSpeak enables users to construct sensor recording applications, location tracking applications, and social networks for things that continuously update their state.

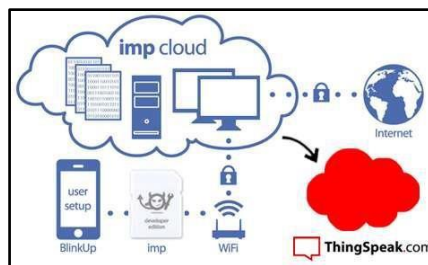


Figure 11: Overview of ThingSpeak (www.thingspeak.com)

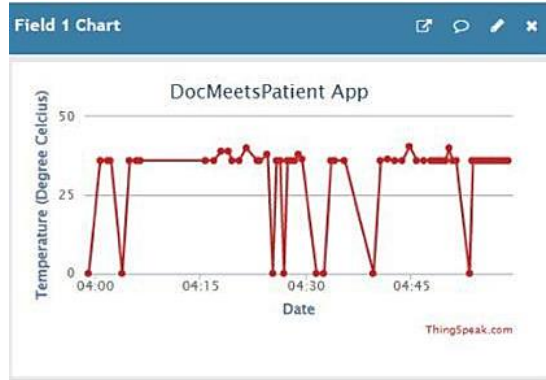
3.0 RESULTS

Based on Figure 12, the smart health monitoring with Internet of Things (IoT) and Arduino has been successfully implemented using an Atmega328 microcontroller that uses Arduino Uno Rev 3. This Arduino serves as the primary controller for the project, allowing it to communicate with all of the gear involved. It is capable of measuring and monitoring fundamental human health by using the LM35 sensor, which functions as a body temperature sensor, and the MAX30100 sensor, which functions as an oximeter sensor, which measures heart rate and detects oxygen levels in the blood. Additionally, the Arduino gathers real-time health data via a MAX30100 sensor that measures heart rate, oxygen levels in the blood, and a temperature sensor that is linked to the Arduino.

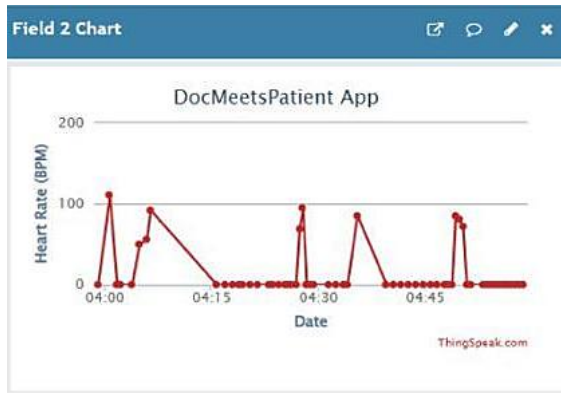


Figure 12: Shows the prototype Smart Health Monitoring System (DocMeetsPatient)

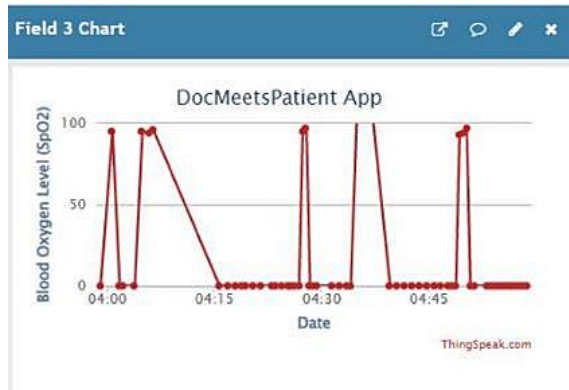
Apart from that, the Arduino is also responsible for collecting, displaying, and transmitting data to the ESP8266, an IoT module, in this project. The common ESP8266 Internet of Things module is linked to the Arduino through a Universal Uniform Transmitter (UART) Receiver, which is responsible for connecting the circuit to the internet and transmitting health data to an IoT (ThingSpeak) server as shown in Figure 13 (a), (b), and (c). This ThingSpeak application is in charge of storing and monitoring medical data. Furthermore, this circuit is capable of not only transmitting health data to a server but also displaying real-time data on a 20x4 LCD. This is advantageous for healthcare workers monitoring patients on-site.



(a)



(b)



(c)

Figure 13: Shows the successful development of the Internet of Things (IoT) for (a) Body Temperature, (b) Heart rate, and (c) Blood Oxygen Level.

Health monitoring is performed non-invasively with this method by simply putting a finger on the sensor and detecting it straight through the skin. Simply by putting a finger on the input sensor, the user will be able to immediately measure and monitor their heart rate, body temperature, and oxygen saturation levels in their blood.

4.0 ANALYSIS

The Smart Health Monitoring System uses the LM35 body temperature sensor, and the MAX30100 pulse oximeter sensor to detect the heart rate and oxygen levels in the blood. From these experiments, 10 reading values were taken from 10 different people to test the level of accuracy of the sensor readings used as shown in Figure 14, Figure 15, and

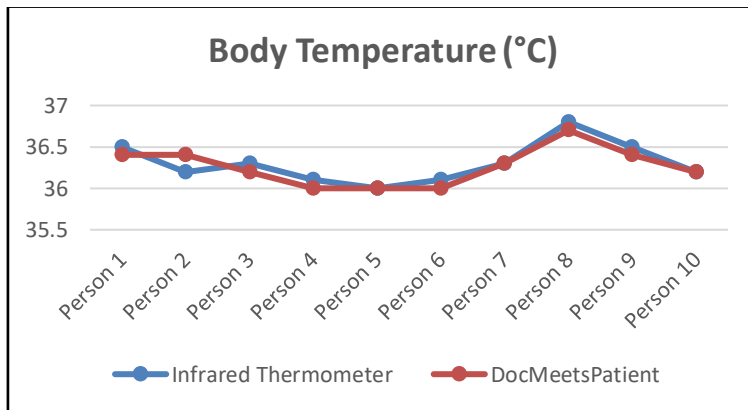


Figure 14: Results of 10 trial sample readings for Body Temperature.

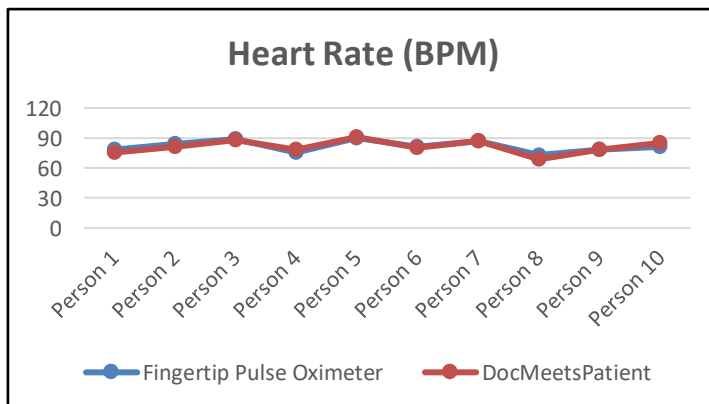


Figure 15: Results of 10 trial sample readings for Heart Rate

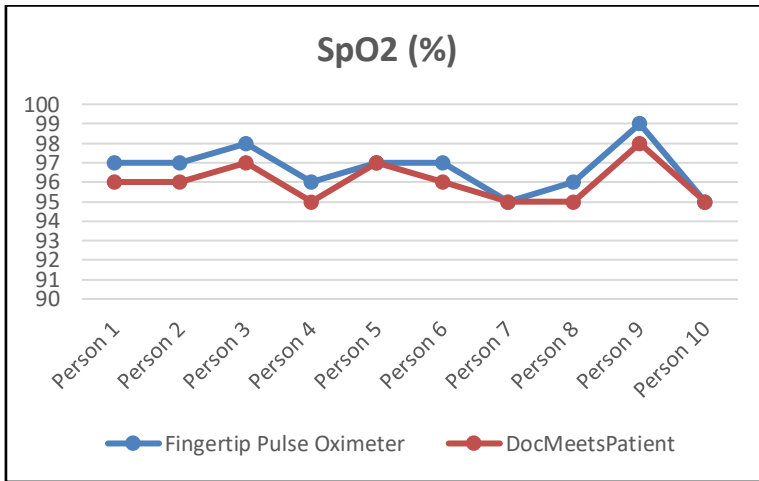


Figure 16: Results of 10 trial sample readings for Blood Oxygen Level



Figure 17: Shows a comparison of body temperature, pulse rate, and blood oxygen levels that have been measured using a real device with readings measured using a designed Smart Health Monitoring System.

Figure 16. Once the testing is carried out, the readings from all these sensors show values that are approximately the same as the purchased measuring instrument (the actual device) as shown in Figure 17. This indicates that the design of a reliable smart health monitoring system has been successfully developed. However, if the finger is not properly placed on the MAX30100 Pulse Oximeter, an erroneous reading may be generated. For pulse rate, only infrared light is needed. Both red light and infrared light are used to measure oxygen levels in the blood. The amount of ambient light hitting the sensor can affect the final value. While using the MAX30100, keep the finger still to avoid an inaccurate reading. Never press the MAX30100 sensor too hard when

using it. This impairs blood flow, resulting in inaccurate readings. To avoid this, insert the finger gently and keep it still, as this will ensure the most accurate reading.

5.0 CONCLUSION

This project is presented to present the construction of a smart health monitoring system by applying the use of Internet of Things (IoT) technology, Android applications, and an Arduino microcontroller. The suggested techniques and approaches operate perfectly and effectively while needing little hardware. The system is suggested to measure a variety of characteristics utilizing sensors such as the LM35 temperature sensor, and the MAX30100 Pulse Oximeter sensor. These sensors are used to detect data on the body temperature, heart rate, and blood oxygen level. By using the IoT platform, health data collected by the three input sensors can be seen on the LCD and in real-time through the ThinkSpeak platform. ThinkSpeak is one example of an IoT platform that will simplify the process of health monitoring on occasion. This developed system provides many facilities for medical staff and families to perform the process of health measurement or monitoring, whether at home or in the hospital.

6.0 ACKNOWLEDGMENTS

The authors would like to thank the Faculty of Electrical and Electronic Engineering Technology (FTKEE), Advanced Digital Signal Processing (ADSP) Lab, Fakulti Kejuruteraan Elektrik (FKE), Universiti Teknikal Malaysia Melaka (UTeM), and Ministry of Higher Education (MOHE), Malaysia that supported this research under project FRGS/1/2020/FTKEE CERIA/F00428.

7.0 REFERENCES

- [1] S. Dharmoji, A. Anigolkar, and P. S. M, "IoT based Patient Health Monitoring using ESP8266," pp. 3619–3624, 2020.
- [2] A. Selvanayakam, A. C. Varishnee, M. Kalaivani, and G. Ranjithkumar, "Health Monitoring System Using IoT," *Lect. Notes Electr. Eng.*, vol. 626, pp. 739–750, 2020, doi: 10.1007/978-981-15-2256-7_68.
- [3] A. Rahaman, M. M. Islam, M. R. Islam, M. S. Sadi, and S.

- Nooruddin, "Developing iot based smart health monitoring systems: A review," *Rev. d'Intelligence Artif.*, vol. 33, no. 6, pp. 435–440, 2019, doi: 10.18280/ria.330605.
- [4] T. Khan and A. Chakrabarty, "Development of Application based Health Monitoring System using GSM module Anika Tasniem 12101081 Nura Jamil 12101007," 2016.
- [5] C. Senthamilarasi, J. J. Rani, B. Vidhya, and H. Aritha, "A Smart Patient Health Monitoring System Using Iot," *Int. J. Pure Appl. Math.*, vol. 119, no. 16, pp. 59–70, 2018.
- [6] A. N. A. Yusuf, F. Y. Zulkifli, and I. W. Mustika, "Development of Monitoring and Health Service Information System to Support Smart Health on Android Platform," 4th Int. Conf. Nano Electron. Res. Educ. Towar. Adv. Imaging Sci. Creat. ICNERE 2018, pp. 3–8, 2019, doi: 10.1109/ICNERE.2018.8642592.
- [7] M. T. A. Mahgoub, O. O. Khalifa, K. A. Sidek, and S. Khan, "Health monitoring system using Pulse Oximeter with remote alert," *Proc. - 2015 Int. Conf. Comput. Control. Networking, Electron. Embed. Syst. Eng. ICCNEEE 2015*, pp. 357–361, 2016, doi: 10.1109/ICCNEEE.2015.7381391.
- [8] L. J. Ramírez López, A. Rodriguez Garcia, and G. Puerta Aponte, "Internet of things in healthcare monitoring to enhance acquisition performance of respiratory disorder sensors," *Int. J. Distrib. Sens. Networks*, vol. 15, no. 5, 2019, doi: 10.1177/1550147719847127.
- [9] E. A. Azman and I. Of, "Final year project report title heartbeat and temperature sensor monitor via mobile phone," 2019.

DOSE MAPPING OF GAMMA IRRADIATION CHAMBER (GIC)

**S. Nur Syafinaz¹, M.R. Mohd Amirul Azrie², A. Nur Amalina² and
M.N. Noramaliza^{2, 3*}**

¹Department of Physics, Faculty of Science
Universiti Putra Malaysia, 43400 Serdang, Selangor, Malaysia

²Medical Physics Unit, Teaching Hospital Universiti Putra Malaysia, 43400 Serdang,
Selangor, Malaysia

³Department of Radiology, Faculty of Medicine and Health Sciences, 43400 Serdang,
Selangor, Malaysia

*Corresponding Author's Email: noramaliza@upm.edu.my

Article History: Received January 24, 2022; Revised January 27, 2022;
Accepted January 27, 2022

ABSTRACT: The use of gamma rays to irradiate blood products have been demonstrated to reduce the probability of post-transfusion graft versus host disease. The aim of this study is to investigate the accuracy of a new batch of Gafchromic EBT-XD films to map the homogeneity of gamma radiation dose delivered to the blood bags and identify the lowest and highest levels of radiation exposure to the blood. The Gammacell 3000 Elan Gamma irradiation chamber (GIC) @ Blood Irradiator with Cesium-137 source was used. During the gamma irradiation at an exposure of 8 minutes 51 seconds to deliver a central dose of 25 Gy to the film, the EBT-XD films were placed at the centre of a blood-equivalent phantom. The doses then were measured using dose mapping analysis of Gafchromic EBT-XD film. The responses of EBT-XD films were compared with EBT3 films and GS 300 Dose Mapping Report 2021 prepared by Best Theratronics Dosimetry Laboratory, Canada. Results showed the value of doses obtained from the mapping using EBT-XD were reliable compared with the doses measured in EBT3 film as they were in the range of the acceptable dose ranges for blood irradiation procedures. The mapping with EBT-XD film yielded a minimum dosage of 18 Gy and a maximum exposure of 32 Gy at 8 minutes 51 seconds of irradiation. In conclusion, EBT-XD offered excellent dosimetric characteristics and has a the potential to dose map the blood irradiator.

KEYWORDS: *Blood irradiator; EBT3 film; EBT-XD film; dosimetry; dose-mapping*

1.0 INTRODUCTION

A way of transferring blood or blood products, from one person to another after blood is lost through an illness or injury is called a blood transfusion. A transfusion generally can help in supplying the replacement or reinforcement to one or more components that make up the healthy blood if the body is missing any one or more of them. Some of the reasons why people might need to receive a blood transfusion are sickle cell disease, a bleeding disorder such as cancer or haemophilia, and anaemia. Patients who suffered from anaemia or an iron deficiency may require a red blood cell transfusion. Platelets are blood cells that aid in the prevention of bleeding. Platelet transfusion is desired if the human body doesn't have enough platelets. This might happen as a result of cancer or cancer treatments. Blood transfusions are generally considered safe, however, there are complications involved. Some issues appear right away, while others take a while.

Transfusion-associated graft-versus-host disease (TA-GVHD) is an uncommon blood transfusion complication in which immunologically competent donor T cells initiate an immune response against the lymphoid tissue of the recipient [1]. In order to prevent the TA-GVHD, the standard method that is currently used in clinical practice is the irradiation of cellular blood products using either gamma rays or X-rays. The purpose of the irradiation is to inactivate the T-lymphocytes found in cellular blood products, preventing blast transformation and mitotic activity [2]. By using gamma irradiation either from Cesium-137 or Cobalt-60, with a minimum dose of 25 Gy, the effect could be achieved.

Prior to actual irradiations being carried-out, the dose mapping analysis using various type of dosimeters are performed to ensure the gamma radiation dose to the blood products are within the specified limits of a minimum of 25 Gy and a maximum of 50 Gy [1]. It is to make sure the given doses are enough to prevent graft versus host disease in even paediatrics and transplant patients. Other than that, the homogeneity of radiation doses on the blood package also need to be performed to ensure the whole blood package received the same exposure regardless at the centre of the package or at the periphery.

Film dosimeter is one of the dosimeters that is oftenly used to map dose in blood irradiator e.g. EBT3 and EBT-XD types. EBT3 film is

made up of a single active layer that contains the active substance, a marker dye, stabilisers, and other additives, resulting in a film with a low energy dependence. The images are acquired with flatbed scanners, EBT3 features a unique polyester substrate that inhibits the development of Newton's Rings interference patterns. While for EBT-XD film in accordance to the product specification notes, it has one active layer, with 25 μm thick. The active layer is symmetrically sandwiched between two 125 μm thick matte polyester substrates. The active layer and the polyester substrates in the EBT-XD film are thinner than those in the EBT3 film (active layer: 28 μm ; polyester substrate: 125 μm) [3].

This study aimed to investigate the uniformity of the dosage of radiation delivered to the blood and to establish the minimum and maximum radiation doses that the blood has been exposed to by using EBT3 and EBT-XD films.

2.0 METHODOLOGY

2.1 Samples preparation, irradiations and dosimetry

In this study, a Gammacell 3000@ Elan Blood Irradiator with Cesium-137 source located at Department of Pathology, Universiti Putra Malaysia was used. The absorbed dose distributions were measured using EBT-XD (Lot #: 08021)- and EBT3 (Lot #: 03071601) radiochromic films (Ashland, US). A blood-equivalent phantom manufactured by Best Theratronics Dosimetry Laboratory, Canada was positioned in the blood canister prior to the irradiation of the films.

2.1.1 Film dose calibration

A total of eight pieces of EBT3 and EBT-XD films were used to obtain dose calibration curves. Prior to irradiation, the films were cut into 11.7 cm \times 19.3 cm and positioned at the centre of the blood-equivalent phantom. Seven pieces of the films were then exposed to gamma-ray with doses ranging from 5 up to 35 Gy, while one film was reserved as a control sample and left unexposed. The dose calibration curves of the films (net OD versus dose) were plotted using three channels (red, green and blue) scan modes in order to choose the best channel to obtain the optimum curves for the films.

2.1.2 Dose Homogeneity

For the dose homogeneity measurements, the films were irradiated at the centre of a blood-equivalent phantom after being positioned in the

blood canister. The irradiation exposure of 8 minutes 51 seconds was used to deliver a central dose of 25 Gy to the film. The number of grids used for mapping was based on the GS Dose Mapping Report 2021 (12 columns, 20 rows). The mapping was done using Origin software for contouring.

2.2 Scanning Protocol and Analysis

All the irradiated films used in this study were scanned after 48 hours post-irradiation using a Microtek ScanMaker 1000 XL (Taiwan) flatbed scanner. The transmission mode was set according to the set-up by [3,4] at the scanner including scan resolution of 75 dots per inch (dpi), a 48-bit TIFF image (16 bits per channel) and all available image correction methods turned off. All film pieces were positioned at the same location in the centre of the scanning area. A 41 cm x 36.1 cm cardboard template was affixed to the scanner to placed films in a repeatable and consistent centre spot on the scan area.

The template was also used to reduce the effect of lateral dependency artefacts (nonuniform readout response induced by light scattering from particles in the film active layer). Five OD measurements were taken across the central region of the scanner to validate this assumption, with a standard error of less than 0.06 per cent.

Distinctive channel values were extracted by using ImageJ v1.49. A region of interest (ROI) of 1.0 cm x 1.0 cm region at the centre of each film was selected. The net OD was calculated as shown in Equation 2.1 [4]:

$$netOD = OD_{exposed} - OD_{unexposed} = \log_{10} \frac{I_{unexposed}}{I_{exposed}} \quad (2.1)$$

where $I_{unexposed}$ and $I_{exposed}$ are the readings for unexposed and exposed film pieces, respectively.

3.0 RESULTS AND DISCUSSION

3.1 Film Dose calibration

The calibration curves obtained for the red, green and blue channels over a dose range from 0 to 35 Gy are shown in Figures 1 and 2. The R-square values, which assess the goodness of the fit, were very close to

unity. Based on Figure 1, as the dose increased, the optical density increased. The growth of the EBT3 red channel was particularly sharp up to around 10 Gy, when the sensitivity was quite strong. The optical density gradually increased at greater doses until it reached saturation. For higher levels of doses, the green channel outperformed the red, indicating that using the green channel at larger doses may be preferable. The green channel showed very high sensitivity and low uncertainty after 25 Gy. Due to the influence of the yellow marker dye, the blue channel of both film types had a smaller response gradient at any dosage. The signal in the blue channel was very slightly affected by the active layer thickness, but the signal in the red channel was significantly affected. Thus, it seemed that the blue channel was less valuable for dose measurement than the green and red channels. Several studies have been published that utilised the blue channel as an optimum analytical approach in triple-channel dosimetry [5,6,7].

For doses more than 5 Gy, EBT-XD films outperformed EBT3 in terms of sensitivity as shown in Figure 2. At doses larger than 10 Gy, the slopes of the response function for the EBT-XD film had a broader dynamic range than those for the EBT3. The red channel of the EBT-XD film was utilized in this research study as it had a wider dynamic range than the EBT3 film. The signal of this channel was much higher than the others.

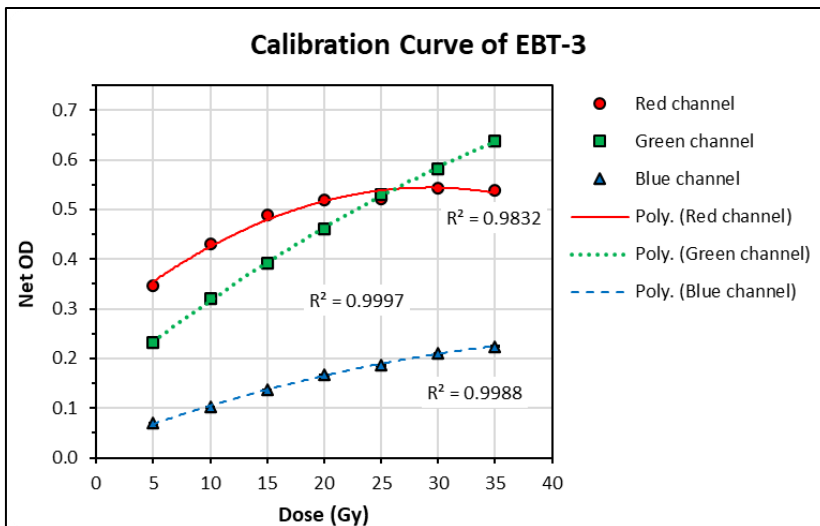


Figure 1: Calibration curve of EBT3 for the red, green and blue channel

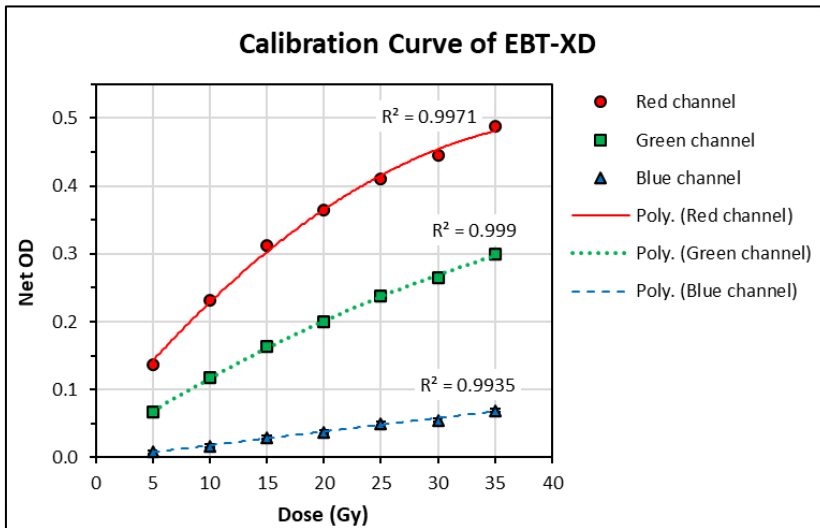


Figure 2: Calibration curve of EBT-XD for the red, green and blue channel

3.2 Dose Homogeneity

The results of the determination of the dose for mapping using the EBT3 and EBT-XD film are shown in Figures 3 and 4. Figure 5 illustrates the dose mapping using radiochromic film from Report 2021.

3.2.1 EBT3 Film

The doses at the peripheral areas of the EBT3 films were greater than 15 Gy as illustrated in Figure 3. However, some area of the central region of the film was less than 25 Gy. These values did not reach the minimum dose required at the centre to eliminate the proliferative of lymphocytes. The minimum central dose required to inactivate the T-lymphocytes was 24 Gy where a measured value of 2400 cGy might range from 2520 cGy to 2380 cGy [2]. Therefore, the use of Gafchromic EBT3 film for dose-mapping of the blood irradiator was not recommended as it was inaccurate.

3.2.2 EBT-XD film

On the other hand, the doses in the peripheral areas of EBT-XD film were greater than 17 Gy. The doses at the central region of the film were between 24 Gy to 25 Gy as shown in Figure 4. The minimum dose obtained was 18 Gy while the maximum dose was 32 Gy. A similar conclusion was reached by Olivo et al 2015 [1] who performed a study on blood irradiation using a linear accelerator. They believed that the

accepted dose range to kill the T-lymphocytes was between 15 Gy to 50 Gy. Hence, Gafchromic EBT-XD film was the most suitable type of film to be used for dosimetry of the blood irradiator. In addition, the pattern of dose mapping for EBT-XD film matched with the Report 2021 displayed in Figure 5. The doses obtained from mapping using both EBT3 and EBT-XD films were in agreement with that obtained from the use of the radiochromic film to within $\pm 8\%$ and $\pm 6\%$ respectively.

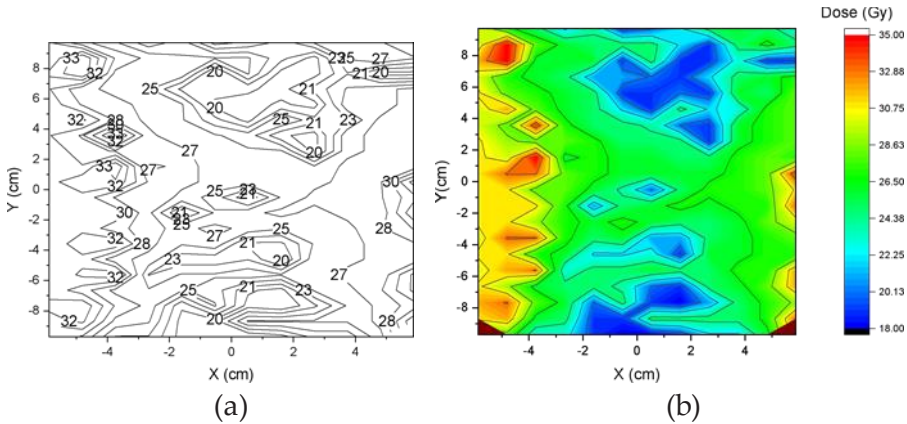


Figure 3: Dose-mapping of a Gammacell 3000 Elan Blood Irradiator using Gafchromic EBT3 film. (a) Contour black and white (b) Contour colour fill

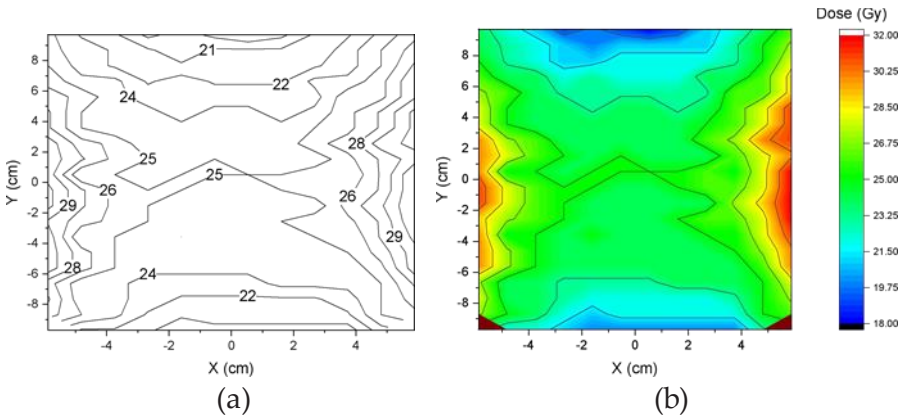


Figure 4: Dose-mapping of a Gammacell 3000 Elan Blood Irradiator using Gafchromic EBT-XD film. (a) Contour black and white (b) Contour colour fill

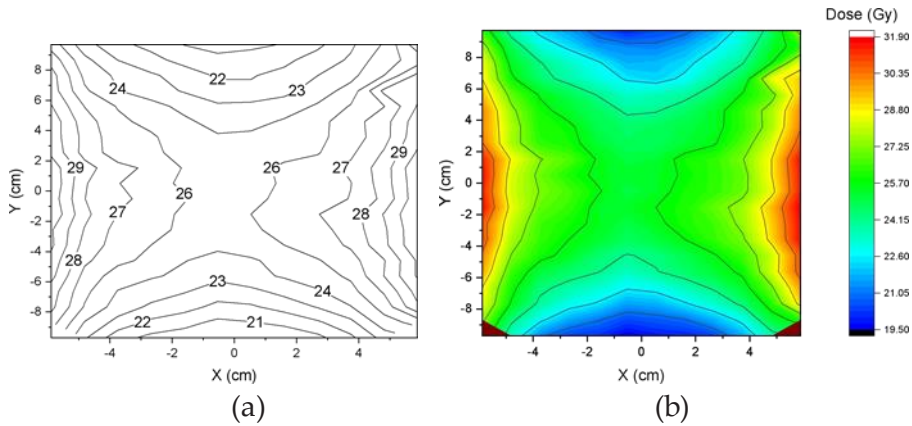


Figure 5: Dose-mapping of a Gammacell 3000 Elan Blood Irradiator using radiochromic film from Report 2021. (a) Contour black and white (b) Contour color fill

4.0 CONCLUSION

The doses in the peripheral areas were observed to be lesser than the central area, for both types of films. EBT-XD film was the most appropriate dosimeter for dose verification compared to EBT3 film. This is due to the fact that for dose-mapping using EBT-XD film, the doses obtained on the film were in the range of doses needed to inhibit the proliferation of the T-lymphocytes as mentioned in [1]. The minimum and maximum dose was 18 Gy and 32 Gy respectively.

5.0 ACKNOWLEDGEMENTS

The authors would like to thank the staff and medical physicists from the Radiology and Pathology Department of Universiti Putra Malaysia Teaching Hospital (HPUPM) for their help in completing this study. The authors also appreciate National Cancer Institute for their help with the scanning of the films.

6.0 REFERENCES

- [1] Olivo, R. A., Silva, M. V. D., Garcia, F. B., Soares, S., Rodrigues, V., & Moraes-Souza, H. (2015). Evaluation of the effectiveness of packed red blood cell irradiation by a linear accelerator. *Revista brasileira de hematologia e hemoterapia*, 37, 153-159.
- [2] Saglam, S., Cakir, A., & Kuter, S. (2011). Blood irradiation. In

Modern Approaches To Quality Control. IntechOpen.

- [3] Casolaro, P. (2021). Radiochromic films for the two-dimensional dose distribution assessment *Applied Sciences*, 11(5), 2132.
- [4] Dreindl, R., Georg, D., & Stock, M. (2014). Radiochromic film dosimetry: considerations on precision and accuracy for EBT2 and EBT3 type films. *Zeitschrift für Medizinische Physik*, 24(2), 153-163.
- [5] Miura, H., Ozawa, S., Hosono, F., Sumida, N., Okazue, T., Yamada, K., & Nagata, Y. (2016). Gafchromic EBT-XD film: dosimetry characterization in high-dose, volumetric-modulated arc therapy. *Journal of Applied Clinical Medical Physics* 17(6), 312-322.
- [6] Mohammadyari, P., Zehtabian, M., Sina, S., Tavasoli, A. R., & Faghihi, R. (2014). Dosimetry of gamma chamber blood irradiator using PAGAT gel dosimeter and Monte Carlo simulations. *Journal of Applied Clinical Medical Physics*, 15(1), 317-330.
- [7] Palmer, A. L., Dimitriadis, A., Nisbet, A., & Clark, C. H. (2015). Evaluation of Gafchromic EBT-XD film, with comparison to EBT3 film, and application in high dose radiotherapy verification. *Physics in Medicine & Biology*, 60(22), 8741.

Penumbra



62

68

72

RED™

REPERFUSION CATHETERS



REDglide™ Technology

Designed to
enhance delivery
in tortuosity



62

.062" ID
1.93mm (0.76") OD
138cm Length

68

.068" ID
2.13mm (0.84") OD
132cm Length

72

.072" ID
2.16mm (0.85") OD
132cm Length

